Far Forward Scattering
of CO_2 Laser Radiation by
Plasma Density Fluctuations
in the W VII-A Stellarator.

C. Mahn

IPP 2/306   February 1990

IPP

MAX-PLANCK-INSTITUT FÜR PLASMAPHYSIK
Garching bei München

Far Forward Scattering
of CO_2 Laser Radiation by
Plasma Density Fluctuations
in the W VII-A Stellarator.

C. Mahn

IPP 2/306 February 1990

Far Forward Scattering
of CO_2 Laser Radiation by
Plasma Density Fluctuations in the W VII-A Stellarator.

Abstract

Far Forward Scattering of CO_2 laser radiation from density fluctuations in the poloidal plane (perpendicular to the main magnetic field) of the $WVII-A$ stellarator plasma results in asymmetric distributions of the beat signals in the detector plane of a *Fourier* lens. It has been attempted to explain the asymmetric profiles with a model which describes scattering from low-M-number quasi-coherent modes, i.e. poloidally propagating periodic density structures of finite radial extent, centered in an annulus possibly near the plasma edge. This is equivalent to the picture of the probing beam being scattered from two waves with identical frequency Ω and center-wavelength Λ_c propagating at two different positions across the beam in nearly opposite directions; the waves have finite lateral extent transverse to their propagation and the wave fronts are not parallel to one another, but rather they are inclined with respect to another. This again means that for one selected fluctuation frequency Ω and one particular mode number M there is a spread in wave numbers $\mathbf{K}$ around $\mathbf{K}_c$. When the beam passes at a finite distance d from the magnetic axis, superimpositioning of the scattered fields results in asymmetric profiles despite a *Klein-Cook* parameter $\gamma \ll 1$.

The mode numbers detected this way range from about 10 to 30; it seems as if there exists for a given magnetic field configuration a maximal mode number which is common to all frequencies, i.e. a mode pattern without a finite group velocity. The question arises whether it is accidental that this number coincides with the periodicity of "islands" which the magnetic field would exhibit at "rational surfaces" near the plasma edge in the case of small disturbances.

We have combined two already existing models, that of laterally extended wave fronts and that of counter-propagating waves. In addition, we included lateral wave front profiles *other than Gaussian ones*, and we introduced the picture of non-parallel fronts.

Finally, EM scattering from fluctuations which are not entirely isotropic, is briefly discussed in general. The advice is given to detect both sidebands also in ordinary Forward Scattering diagnostics, because their intensity ratio is a measure of the degree of isotropy of the fluctuations.

Contents

1. Introduction

Fluctuations of density and fields in tokamak and stellarator plasmas are in the focus of interest because of their possible influence on particle and energy loss mechanisms. The two main diagnostics involved are Langmuir probes and scattering of electromagnetic (EM) waves. Probes offer the advantage of being capable of detecting both density and electric field fluctuations (and the phase between them) but, for technical reasons, they can only be applied in dilute plasmas (e.g. edge plasmas) . Not restricted by damage threshold but requiring more technology is the more recently developed third method: scattering of heavy ion beams, which also yields information on density and field fluctuations /1/. The EM waves scattering technique, on the other hand, can only detect density fluctuations but causes no disturbance whatsoever and is applicable to any relevant plasma region. While probes and EM scattering have been widely used in *tokamak* plasmas /2/, there are not many publications on scattering from *stellarator* plasmas /3/,/4/.

This report attempts to interpret some experimental findings in scattering with CO_2 laser radiation from density fluctuations in $WVII-A$ stellarator plasmas /5/,/6/. While originally designed to detect density fluctuation wavelengths in the order of mm by forward scattering and homodyning with a local oscillator, in the course of the experiment it turned out that this scattering is dominated by the existance of longer wavelengths (order of cm). In this case the scattering angle is very small and within the divergence of the probing beam; the scattered fields then mix with the field of the probing beam.

This *small angle forward scattering* has been proposed /7/ and extensively treated /8/ by *M. v. Hellermann et al.*, and it has been tested /7/ and applied to tokamak plasmas /9/. The technique is to select a beat frequency and scan its amplitude across the diameter of the beam after passage of the plasma. This profile, the result of the interaction of the scattered EM sideband fields with that of the probing beam, is expected to be symmetric with respect to the beam axis as long as the sideband fields are symmetric (the profile of the beam itself being assumed to be *Gaussian*). As a matter of fact, the profile is reported to be occasionally asymmetric /9/ and possible explanations for this have been proposed /10/,/11/. Under *W VII-A* conditions most of the recorded profiles proved to be asymmetric. In the following a model is presented that – with reference to /8/ – combines the effects of finite lateral extent and counter-propagation of density waves on EM scattering, and also takes into account the inclination of the wave fronts with respect to each other. Such a model might describe quasicoherent poloidal modes in an annular layer of toroidal devices such as *tokamaks* and *stellarators* . In particular, when adjusted to the elliptical shape of the plasma cross-section due to the $l = 2$ helical winding configuration, the model can reproduce the asymmetric profiles found in this *Wendelstein* stellarator.

An outline of the general FFS scheme is given in Section 2; the modified model is described in Section 3, the first part of which treats the case of one wave, and the second part two counter-propagating waves. Finally, some results are presented in Section 4.

2.1. Some Definitions

Density fluctuations with wavelengths larger than the *Debye* length are entitled collective; although predominantly the electrons scatter EM radiation, the frequency spectrum of the radiation scattered from them is determined by the motion of the ions. Scattering of coherent EM radiation from collective density fluctuations (occasionally called "*collective*" or "*coherent*" scattering) is in general accomplished by superimpositioning, i.e. superimposed on the low-amplitude scattered fields is the field of a so-called "*local oscillator*" (LO) of either the same frequency (as that of the incident beam) – "*homodyning*" – or a shifted frequency – "*heterodyning*". The EM frequency ω of the "*probing beam*", the "*carrier*" field T, is *Doppler*-shifted in the scattered fields, the "*sideband*" fields S: $\omega \pm \Omega$ ($\Omega \ll \omega$); and it is the "*beat*" (or "*intermediate*") frequency Ω that represents the *frequency* of the density fluctuations. Since in most applications of scattering from collective fluctuations, the EM wavelength λ is somewhat smaller than that of the fluctuation and scattering consequently then occurs in the forward direction, we will denote the scattering technique with an external LO as "*forward scattering*" (FS: $\lambda < \Lambda$; external LO). When the EM wavelength is much smaller than that of the fluctuation, Λ, and the scattering angle therefor is very small and within the divergence of the probing beam, an external beam is not necessary as LO, because the scattered fields are superimposed on the field of the probing beam itself: "*far forward scattering*" (FFS: $\lambda \ll \Lambda$; self-mixing). *) In this case the *wavelength* Λ (wave number $K = \frac{2\pi}{\Lambda}$ and frequency Ω) has to be obtained by a "*curve-fitting*" procedure; it cannot be derived from the scattering angle via momentum transfer, as is done for larger angles, because at such small angles both "sidebands" (the "*red*" and "*blue*" ones or the "*left*" and the "*right*" respectively) are rather broad in angle (poor K-resolution) and overlap. For that goal one derives the sideband EM fields S for the particular situation, superimposes them on the carrier EM field T and formulates the resulting intensity profile I in the detector plane, the "K - *space profile*". This profile is the distribution of amplitudes at the "beat" frequency Ω across the probing beam and is characterized by two parameters: the wavevector K of the fluctuation and its axial position z along the probing beam. The position across the beam in the detector plane is measured in form of the normalized co-ordinate u, the wavevector in form of the normalized parameter v and the axial position in form of the normalized parameter ς; so the profile has the form $I(u; v, \varsigma)$.

---

*) There is some confusion in the literature: occasionally the term "*homodyning*" is applied to *this* situation ("self-mixing"), while "*heterodyning*" then refers to the use of an *external* LO. Naturally, "self-mixing" can only be run in the "*homodyning*" mode in the above sense.

2.2. A Brief Review of *Far Forward Scattering* (FFS)

is necessary in order to explain how in this paper the existing theory is adapted to the modelling of macroscopic density structures in the poloidal plane of the $WVII - AS$ plasma.

The treatment of FFS /7/ is based exclusively on refraction and diffraction: The interaction of the EM wave with a density fluctuating phase object is represented by refraction; the EM field amplitude distribution in the detector plane is related to that one in the object plane by diffraction (in the "slim beam" *Fresnel* approximation). The probing EM beam is assumed to be a *Gaussian*, propagating along z in *Cartesien* co-ordinates, and the phase object to be propagating across the beam, nearly along x: **Fig. 1**.
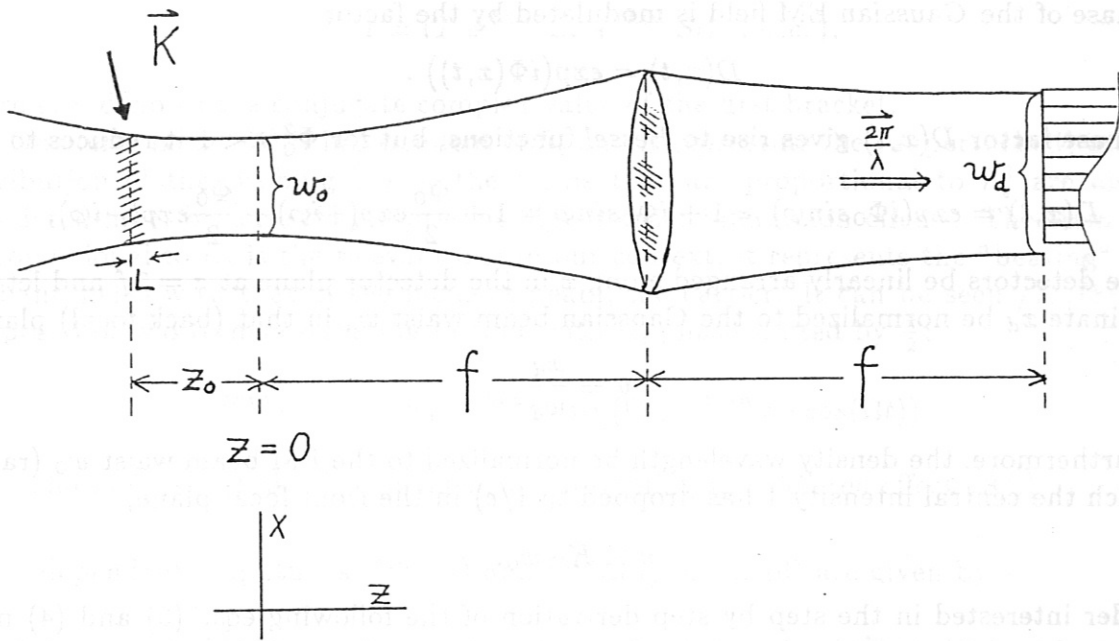

Fig. 1. *FFS: A Gaussian beam propagates from left to right along the z-axis, and the phase disturbance with wave vector $\vec{K}$ occurs in the object plane, a distance z from the beam waist ($z = 0$), which is in the front focal plane of a lens. In its back focal plane ($z = $ twice the focal length f) a detector array is located (detector plane). L is measured perpendicular to $\vec{K}$ and is the lateral width of the density wave front.*

For a given scattering angle ($\approx \lambda/\Lambda$) there is a critical lateral width L of the density wave Λ; as long as L does not exceed this value, i. e. $\frac{L \cdot \lambda}{\Lambda^2} << 1$, the phase disturbance may be treated as a 2-dimensional phase-screen in the object plane ("*Raman-Nath*" scattering: "*thin grating*" or "*thin layer*") /8/.

Let the electron density fluctuation $\tilde{\nu}_e$ be independent of y (perpendicular to the plane of **Fig. 1**), and let us assume that the scattering object is a density fluctuation in a plasma; furthermore, that the "line-integrated" fluctuation level along z,

$$L \cdot \tilde{n}_e = \int_{-\infty}^{+\infty} \tilde{\nu}_e(z)dz \, ,$$

originates from a lateral width L small enough in the sense mentioned above.

The index of refraction of a plasma then fluctuates, causing a fluctuating phase shift of the probing EM field with an amplitude

$$\Phi_0 = r_e \cdot \lambda \cdot L \cdot \tilde{n}_e \quad (r_e \text{ is the classical electron radius}) \, .$$

In case this fluctuation is a "monochromatic" wave, propagating across the beam along x :

$$\Phi(x,t) = \Phi_0 \cdot \sin \varphi(x,t) \quad , \text{with} \quad \varphi(x,t) = Kx - \Omega t \, ,$$

the phase of the *Gaussian* EM field is modulated by the factor

$$D(x,t) = exp\big(i\Phi(x,t)\big) \, . \tag{1}$$

The phase factor $D(x,t)$ gives rise to *Bessel* functions, but for $\Phi_0^2 << 1$ it reduces to

$$D(x,t) = exp(i\Phi_0 sin\varphi) \approx 1 + i\Phi_0 sin\varphi = 1 + \frac{\Phi_0}{2} exp(+i\varphi) - \frac{\Phi_0}{2} exp(-i\varphi). \tag{2}$$

Let the detectors be linearly arranged along x in the detector plane at $z = 2f$ and let this co-ordinate x_d be normalized to the Gaussian beam waist w_d in that (back focal) plane:

$$u \equiv \frac{x_d}{w_d}.$$

Let, furthermore, the density wavelength be normalized to the EM beam waist w_0 (radius at which the central intensity 1 has dropped to $1/e$) in the front focal plane,

$$v \equiv K \cdot w_0.$$

A reader interested in the step by step derivation of the following eqs. (3) and (4) must be referred to / 7/ or / 8/, where it is shown that the small amplitude phase modulation around $D(x,t) = 1.$ in eq. (2) results in scattered EM fields that are sidebands S of the probing EM field; they are shifted in spatial and in temporal frequencies, and these sideband amplitudes (e.g. in V/cm) in the case of small phase disturbances are equivalent to the $+1$ and -1 diffraction orders caused by a moving sinoidal phase grating. Related to the detector plane and valid for a "thin layer" approximation, they are:

$$^{thin}S_{l,r} = \mp E_0 \cdot \Phi_0 \cdot exp\big(-\frac{1}{2}(u \pm v)^2(1 - i\varsigma)\big) \cdot exp(\pm i\Omega t). \tag{3}$$

The nearly unperturbed phase $D(x,t) \approx 1.$ in eq. (2), on the other hand, amounts to a nearly unperturbed field amplitude of the probing beam, the carrier T:

$$T = E_0 \cdot exp\big(-\frac{1}{2}u^2(1 - i\varsigma)\big). \tag{4}$$

The fast time dependence $exp(i\omega t)$ of the EM field in the terms S and T has been omitted: the detector electronics will not resolve it. The argument $i\varsigma$ in this complex notation reflects the curvature of the EM wave fronts.

4

In eqs.(3) and (4) the position at the z-axis has been normalized to the *Rayleigh* length:

$$\varsigma \equiv z/z_R \quad ; \quad z_R = 2\pi w_0^2/\lambda.$$

The upper sign in eq. (3) refers to the "right" (index "r") and the lower sign to the "left" (index "l") sideband.

The field pattern of eq. (3) in the detector plane x_d, y_d is the spatial *Fourier* transform of the field patterns in the object plane x, y; superposition on T (eq. (4)) then leads to the K-*space* profile.

Using a square law detector amounts to squaring of the superimposed fields, i. e. the intensity (power density flow, e.g. in $\frac{W}{cm^2}$) of the emerging beam in the detector plane is:

$$^{thin}I = (T +^{thin} S_r +^{thin} S_l) \cdot (c.c.), \tag{5}$$

where $c.c.$ denotes the conjugate complex value of the first bracket.

One term in eq. (5) is independent of $\tilde{n}_e$ and it represents the (unperturbed) intensity distribution of the probing beam; the terms that are proportional to $\tilde{n}_e^2$ are also not considered here, because they represent higher-order interaction effects. The term which is proportional to $\tilde{n}_e$ is the relevant one in our context; it represents the "beating" of the sideband fields with that of the incident beam, the carrier. It can be seen /7/,/8/ to be composed of two terms oscillating in time with Ω, phase shifted by $\frac{\pi}{2}$:

$$^{thin}I = E_0^2 \cdot \Phi_0 \cdot (^{thin}g \cdot sin(\Omega t) +^{thin} h \cdot cos(\Omega t)). \tag{6}$$

(For values of $v << 1$ this is equivalent to an oscillating *Schlieren* effect /8/.)

The u-dependent amplitudes $^{thin}g(u)$ and $^{thin}h(u)$ in eq. (6) are given by

$$^{thin}g \cdot exp(+\frac{1}{4}v^2) = exp(-(u-\frac{v}{2})^2) \cdot sin(\epsilon_+) + exp(-(u+\frac{v}{2})^2) \cdot sin(\epsilon_-), \tag{7a}$$

$$^{thin}h \cdot exp(+\frac{1}{4}v^2) = exp(-(u-\frac{v}{2})^2) \cdot cos(\epsilon_+) - exp(-(u+\frac{v}{2})^2) \cdot cos(\epsilon_-), \tag{7b}$$

where the abbreviation

$$\epsilon_\mp \equiv v^2\varsigma(\frac{1}{2} \pm \frac{u}{v})$$

has been used. In practice one measures the envelope of these amplitudes (the AC signal at frequency Ω is rectified and then time-averaged in $\Delta T \gg \frac{2\pi}{\Omega}$):

$$^{thin}I_{mix}(u) = E_0^2 \cdot \Phi_0 \cdot exp(-\frac{1}{4}v^2) \cdot \sqrt{(^{thin}g)^2 + (^{thin}h)^2}, \tag{8}$$

which is a function of position u, with v and ς as parameter. This eventually is what we have defined as K-*space* profile; in this "thin layer" approximation it is symmetric about $u = 0$: $^{thin}I_{mix}(-u) = {}^{thin}I_{mix}(+u)$.

5

However, as mentioned before, measured profiles in *tokamaks* and *stellarators* tend to be asymmetric about $u = 0$. This result has been tried to explain in two ways.

M. v. Hellermann /8/,/10/ outlined the influence from a finite lateral extent L (or "thickness") of the wave (i.e. the case where the condition $\frac{L \cdot \lambda}{\Lambda^2} << 1$ is no longer valid). For that purpose the differential equation describing the propagation of a *plane* EM wave in a plasma modulated by a "monochromatic" density wave was solved approximately, the lateral amplitude distribution of the latter being *Gaussian* in shape. This results in "damping" of the sideband field amplitudes, which renders them asymmetric:

$$^{thick}S_{l,r} = {}^{thin}S_{l,r} \cdot exp\left(-\left(\gamma(\frac{1}{2} \pm \sigma)\right)^2\right),\tag{9}$$

with

$$\gamma = v^2 \frac{L}{z_R cos\psi} \quad , \quad v = \frac{2\pi w_0}{\Lambda cos\psi}\tag{9a}$$

and

$$\sigma = \frac{\Lambda sin\psi}{\lambda}.\tag{9b}$$

(γ, the *Klein-Cook* parameter, is almost identical with the value of $\frac{L \cdot \lambda}{\Lambda^2}$ mentioned above. It characterizes the scattering regime, $\gamma \ll 1$ denoting the "thin layer" or *Raman-Nath* approximation, $\gamma \geq 1$ the "volume effect" or *Bragg* regime.) ψ is the angle of incidence, i.e. between the density wave front and the EM wave vector $\vec{k}$, which has the beam direction. So two more parameters enter into the K-space profile $^{thick}I(u)$: the thickness L and the angle ψ, henceforth called the angle of irradiation.

Similarly, *Sonoda et al.* /11/ presented a strict volume integration over the entire interaction region - thus including an arbitrary lateral extent of the density wave - , though their explicit analytical results again refer to a *Gaussian* shape of that lateral profile (they compared their calculations with results from microwave scattering from ion-acoustic waves launched into a low-pressure d.c. discharge plasma).

The conditions for CO_2 laser scattering at *W VII-A* however, are characterized by $\gamma \ll 1$ (*Raman-Nath* scattering), unless unreasonably large values of L are assumed (layer lengths L a multiple of the wavelength Λ). This means that the observed asymmetries cannot be explained in this way.

Therefore, as a second approach another model was tried: The probing EM beam intersects two identical density waves travelling in different layers and in opposite directions; asymmetries will then be caused by the phase difference between these waves /8/,/12/. This could not explain the *W VII-A* results either, as long as these layers were taken as thin and plane.

For all these reasons we present here another model of the small **K** density fluctuations in toroidal plasma devices. It combines the picture of a finite lateral extent with that of counter-propagation of density waves. In addition, this model is more flexible inasmuch as it allows for *arbitrary* lateral amplitude distributions and also for an inclination of the density wave fronts with respect to each other, such as might be the case in for instance, poloidally bent density waves of finite radial thickness. And it turns out that this picture eventually suffices to explain the data.

6

3. The Model

Though the relevant results from tokamaks in generally suggest microfluctuations /2/ turbulent to a degree that might exclude their being assumed to be treatable as a composition of linear waves, the proposal of this model is nevertheless motivated by the suggestion that there is not only a *fine-grain* structure of microfluctuations that might be highly turbulent and isotropic, but also a *coarse-grain* structure which is mode-like, and that there exist plasma regions (e.g. the edge) where the latter prevails in amplitude. This hypothesis is supported by some tokamak results /13/,/14/,/15/, where coherent phenomena have been observed.

The model deals with scattering from density fluctuations in a poloidal cross-section of a tokamak or stellarator plasma, i.e. propagating perpendicular to the main magnetic field. Within this plane it assumes poloidally periodic density variations, with radial periods comparable to the poloidal ones ($|\vec{K}_r| \approx |\vec{K}_\phi|$), settled in a layer somewhere between the pressure gradient and the edge region. A probing EM beam will thus traverse this layer twice when passing not too far from the magnetic axis (see **Fig. 2**).
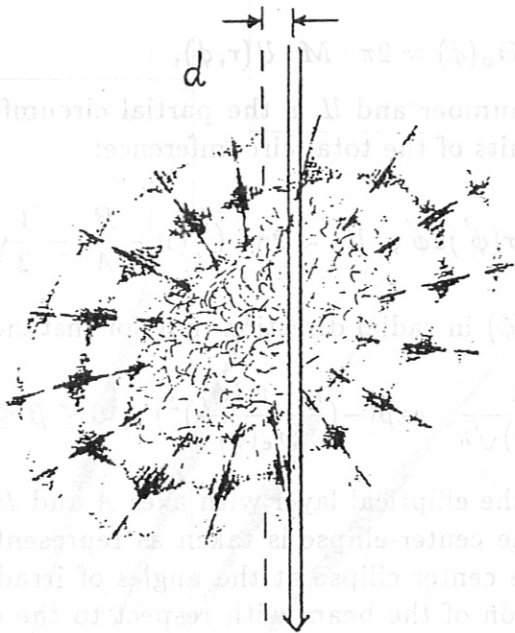

Fig. 2: *An EM beam is scattered from fluctuations of the electron density of a plasma confined in a toroidal magnetic field. As indicated in this poloidal cross-section (perpendicular to the confining field), the model assumes that part of these fluctuations is anisotropic in the form of poloidal modes of frequency Ω, and with wavelengths Λ that cause scattering in the FFS domain: The beam emerges with amplitudes and phases slightly altered at the "beat" frequency Ω. If the probing beam traverses this mode structure displaced by an amount d from the center, the **K**-space profile at frequency Ω becomes asymmetric.*

7

In particular, for the $WV II - A$ stellarator this implies: The cross sections of the magnetic flux surfaces are nearly concentric ellipses of constant excentricity; in polar coordinates r and ϕ:

$$r^2(\phi) = \frac{1 - \epsilon^2}{1 - \epsilon^2 \cdot \cos^2\phi}$$

($\epsilon = 1 - B^2/A^2$; B and A the minor and major axes; r in units of A)

The mode structure of the density fluctuations in the poloidal plane is accordingly modelled by the *ad hoc* assumption:

$$\tilde{\nu}_e(r,\phi,t) = \mathcal{N}(r,\phi) \cdot exp(-i(\Omega t - \Theta_\phi(\phi))),$$

where the poloidal phase $\Theta_\phi(\phi)$ is characterized by two features:

1) the wavefronts are inclined towards the center: $\frac{\vartheta\Theta_\phi}{\vartheta r} = 0$,

2) the wavelength Λ_ϕ along the ellipse $r(\phi)$ is constant: $\frac{\vartheta K_\phi}{\vartheta\phi} = 0$.

Thus the phase is given by

$$\Theta_\phi(\phi) = 2\pi \cdot M \cdot \mathcal{U}(r,\phi),$$

where M is the poloidal mode number and $\mathcal{U}$ is the partial circumference of the ellipse between 0 and ϕ, measured in units of the total circumference:

$$\mathcal{U}(r,\phi) = \frac{1}{\mathcal{U}_0} \cdot \int_0^\phi r(\phi')d\phi'; \quad \mathcal{U}_0 \approx 2\pi \cdot \left(\frac{3}{4}(1 + \frac{B}{A}) - \frac{1}{2}\sqrt{\frac{B}{A}}\right).$$

The amplitude distribution $\mathcal{N}(r,\phi)$ in radial direction may for instance be a *Gaussian*:

$$\mathcal{N}(r,\phi) = \frac{A}{\beta r_c(\phi)\sqrt{\pi}} \cdot exp\left(-\left(\frac{r - r_c(\phi)}{\beta r_c(\phi)}\right)^2\right) \, , \, 0 \leq \beta \leq 1,$$

$r_c(\phi)$ being the center-ellipse of the elliptical layer with axes A and B.

The wavelength Λ_c along the center-ellipse is taken as representative for the mode. The probing beam intersects the center-ellipse at the angles of irradiation [1,2]ψ_c. These angles are given by the orientation of the beam with respect to the ellipse, in particular by its displacement d from the center.

The goal is to derive the **K**-*space* profile in dependence of the the distance d and of the thickness L by evaluating the side bands in analogy to eq. (9).

Confronted with the task to describe the interaction of the probing EM beam with this density structure, we retreat to a simplified approach of superpositioning elementary waves.

We shall first derive the EM fields scattered from each of the two intersections: scattering from a laterally extended density wave with non-parallel fronts ("one wave"). Thereafter we shall treat the interaction the two: scattering from two locally separated, extended and almost identical density waves that propagate in almost opposite directions ("two counter-propagating waves").

8

One wave:

The lateral profile of the density wave may be characterized by its center r_c and its half amplitude half width L, – now permitted to be thicker than consistent with the phase screen conception.

This profile is subdivided into N_n sublayers (**Fig. 3**). The particular kind of subdivision and its indication of course is of no concern; for practical reasons we have chosen the width l_n of the sublayers to decrease in geometric order with the integer n:

$$l_n = \frac{L}{2^n} \; ; \; n = 0, 1, 2, 3, ...; \quad (l_0 = L, \; l_1 = \frac{1}{2}L, \; l_2 = ...).$$

The number of sublayers accordingly is $N_n = 2^{n+2} + 1$ ($N_0 = 5$, $N_1 = 9$, $N_2 = ...$), each of them centered at r_k and characterized by an index k which runs from 1 at one side of the density profile to N_n on the other side: $k = 1, 2, 3, ..., N_n$. $k_c = 2^{n+1} + 1$ is the index for the central sublayer at r_c.
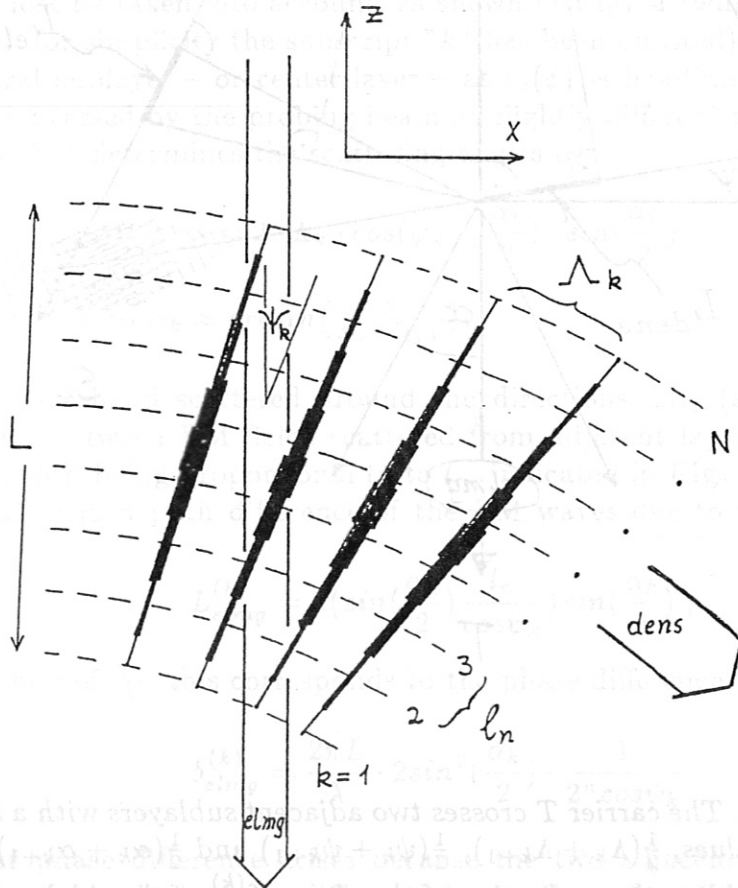

Fig. 3 : *The model: The fronts of the propagating density wave ("dens") may be non-parallel; their amplitude profile (indicated by different thicknesses) is replaced by N discrete values a_k (with $\sum a_k = 1$). So in this picture the EM probe beam ("elmg") intersects at different angles ψ_k N sublayers with different wavelengths Λ_k.*
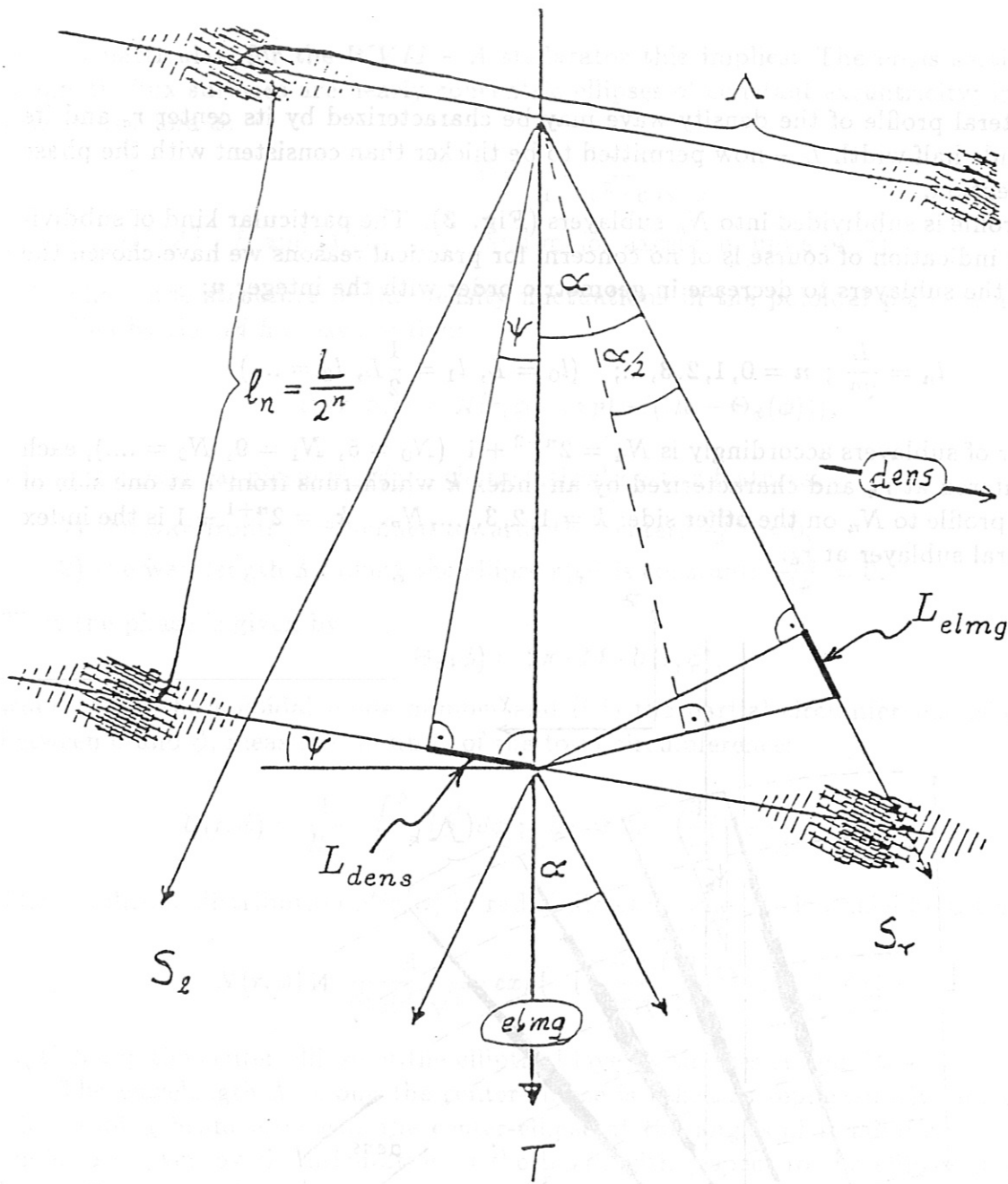
Fig. 4: *Detail of Fig* **3**. *The carrier* T *crosses two adjacent sublayers with a separation* l_n. Λ, ψ *and* α *are mean values,* $\frac{1}{2}(\Lambda_k + \Lambda_{k+1})$, $\frac{1}{2}(\psi_k + \psi_{k+1})$ *and* $\frac{1}{2}(\alpha_k + \alpha_{k+1})$ *respectively. The figure serves to elucidate the evaluation of the phases* $\delta_\pm^{(k)}$ *of the sidebands in eq.* (12).

For the purpose of tayloring symmetric profiles it is convenient to transform from r_k to the co-ordinate ρ_k which is the distance between the sublayer centered at r_k and the central sublayer centered at r_c:

$$\rho_k \equiv r_k - r_c = (k - k_c) \cdot l_n.$$

(For instance with $n = 1$ the 9 sublayers of thickness $\frac{L}{2}$ are centered at $\rho_1 = -2L$, $\rho_2 = -\frac{3}{2}L$, ..., $\rho_5 = 0$, ..., $\rho_8 = +\frac{3}{2}L$, $\rho_9 = +2L$.)

In this heuristic and elementary approach the 3-dimensional phase structure is thus represented by N_n locally separated phase screens k with different amplitudes a_k and a phase factor $D(x,t)$ of the type in eq. (1) and (2). Their wavelength Λ_k and their angle of irradiation ψ_k varies with radius r_k. And since in this FFS configuration there is no spatial resolution, the situation can be looked at as scattering from a system with "spatial dispersion": Not only one single $\mathbf{K}$, but apparently a whole group of wave numbers contribute to the scattering signal at a given Ω. When superimposing the scattered fields, their phases must be taken into account, as shown in **Fig. 4** (which is a detail from **Fig. 3** and in which for simplicity the subscript "k" has been omitted).

The central sublayer – or center-layer – at $r_c(\phi)$ is irradiated at ψ_c, and the other sublayers are traversed by the probing beam at slightly different angles of irradiation ψ_k; Λ_k together with λ determines the scattering angles α_k:

$$\lambda = 2 \cdot \Lambda_k \cdot cos(\psi_k - \frac{\alpha_k}{2}) \cdot sin(\frac{\alpha_k}{2}). \qquad (10a)$$

At FFS this reduces to $\alpha_k \approx arcsin(\frac{\lambda}{\Lambda_k \cdot cos\psi_k})$.

For either sideband scattered around the directions $\pm\alpha_c$ (at the center-layer) the phase difference between EM fields scattered from adjacent layers k and $k + 1$ has two contributions, both being proportional to to l_n, indicated in **Fig. 4**.

One stems from a path difference of the EM waves due to their finite propagation velocity:

$$L_{elmg}^{(k)} = 2\big(sin(\frac{\alpha_k}{2}) \frac{l_n}{cos\psi_k}\big) sin(\frac{\alpha_k}{2}) ;$$

measured in units of $\frac{2\pi}{\lambda}$, this corresponds to the phase difference

$$\delta_{elmg}^{(k)} = \frac{2\pi L}{\lambda} \cdot 2sin^2(\frac{\alpha_k}{2}) \cdot \frac{1}{2^n cos\psi_k}.$$

The other phase difference arises because the two adjacent density "gratings" are encountered by the probe beam in different phases: From $\Phi = \Phi_0 \cdot sin(Kx - \Omega t)$ it follows that a change from x to $x + dx$ causes a relative change in phases of $\frac{d\Phi}{\Phi_0} = K \cdot dx$; thus with

$$dx \equiv L_{dens}^{(k)} = l_n \cdot tg\psi_k \quad \text{this amounts to} \quad \delta_{dens}^{(k)} = \frac{2\pi L}{\Lambda_k} \cdot \frac{tg\psi_k}{2^n} .$$

Hence the net phase difference between EM waves scattered from adjacent sublayers is

$$^{Bragg}\delta_{\pm}^{(k)} \equiv \delta_{elmg}^{(k)} \mp \delta_{dens}^{(k)} = \frac{\Lambda_k}{\lambda} \cdot \left(\frac{\Lambda_k}{\lambda} 2\sin^2\left(\frac{\alpha_k}{2}\right) \mp \sin\psi_k \right) \cdot \cos^2\psi_k \cdot \gamma_k , \qquad (10)$$

where, – by analogy with eq. (9a) –

$$\gamma_k = v_k^2 \cdot \frac{L}{z_R \cdot \cos\psi_k} \quad ; \quad v_k = \frac{2\pi w_0}{\Lambda_k \cdot \cos\psi_k} \cdot \qquad (11)$$

We relate all phases to that of the center-layer; that means that they are made up by the sum of the phase differences:

$$\delta_{\pm}^{(k)} = \pm \sum_{\kappa=k_c}^{k} {}^{Bragg}\delta_{\pm}^{(\kappa)}. \qquad (12)$$

N_n different sideband fields of the type in eq. (3) are being scattered from the N_n different sublayers, each sideband field being characterized by another v_k:

$$^{thin}S_{l,r}{}^{k} = \mp E_0 \cdot \Phi_0 \cdot exp\left(-\frac{1}{2}(u \pm v_k)^2(1 - i\varsigma)\right) \cdot exp(\pm i\Omega t). \qquad (3a)$$

The phases in eq. (12) must be attached to the sublayer sideband fields in eq. (3a) before superimpositioning:

$$S_{l,r} = \sum_{k=1}^{N_n} {}^{thin}S_{l,r}{}^{k} \cdot \frac{a_k}{2} \cdot exp(+i\delta_{\pm}^{(k)}) \text{ , with } \sum_{k=1}^{N_n} a_k = 1 . \qquad (13)$$

Equation (13) is equivalent to eq. (9): it represents the sideband fields modified by the "volume effect". The lateral amplitude profile a_k of the density wave front can be shaped arbitrarily; for a *Gaussian* profile, for instance one has $a_k = \frac{1}{2^n} exp(-(1.6651\frac{\rho_k}{L})^2)$.

(When all wavefronts are parallel, all phase differences in eq. (10) are of the same value $^{Bragg}\delta_{\pm}^{(c)}$, and hence $\delta_{\pm}^{(k)} = \pm(k - k_c) \cdot^{Bragg}\delta_{\pm}^{(c)}$. It turns out that the thicker the layer, the more narrowly will the scattered intensity be concentrated around an angle ψ_c that corresponds to $^{Bragg}\delta_{+}^{(c)} = 0$; this is the well-known *Bragg* angle $(\psi_c)_0 \equiv \psi_{Bragg}$, which is characterized by $\psi_{Bragg} = \frac{1}{2}\alpha_{Bragg}$ and $\lambda = 2\Lambda_c \sin\psi_{Bragg}$: inserted into eq. (10), the upper sign yields $^{Bragg}\delta_{+}^{(c)} = 0$. See also Appendix 1 and **Fig.A2** in Appendix 2 !)

12

The side bands $S_{l,r}$ being calculated in eq. (13), the carrier field T remaining the same as in eq. (4):

$$T = E_0 \cdot exp\left(-\frac{1}{2}u^2(1 - i\varsigma)\right),$$

— the result of superimpositioning the fields $S_{l,r}$, eq. (13), and T, eq. (4), must be squared as in eq. (5):

$$I = (T + S_r + S_l) \cdot (c.c.);$$

and after some manipulation this results to a form analogous to eq. (6) :

$$I = E_0^2 \cdot \Phi_0 \cdot \left(g \cdot sin(\Omega t) + h \cdot cos(\Omega t)\right), \tag{14}$$

with

$$g = +\sum_{k=1}^{N_n} exp\left(-\frac{1}{2}\left(u^2 + (u - v_k)^2\right)\right) \cdot a_k \cdot sin\left(-\frac{1}{2}\varsigma\left(u^2 - (u - v_k)^2\right) + \delta_+^{(k)}\right)$$

$$+\sum_{k=1}^{N_n} exp\left(-\frac{1}{2}\left(u^2 + (u + v_k)^2\right)\right) \cdot a_k \cdot sin\left(-\frac{1}{2}\varsigma\left(u^2 - (u + v_k)^2\right) + \delta_-^{(k)}\right), \tag{15a}$$

$$h = +\sum_{k=1}^{N_n} exp\left(-\frac{1}{2}\left(u^2 + (u - v_k)^2\right)\right) \cdot a_k \cdot cos\left(-\frac{1}{2}\varsigma\left(u^2 - (u - v_k)^2\right) + \delta_+^{(k)}\right)$$

$$-\sum_{k=1}^{N_n} exp\left(-\frac{1}{2}\left(u^2 + (u + v_k)^2\right)\right) \cdot a_k \cdot cos\left(-\frac{1}{2}\varsigma\left(u^2 - (u + v_k)^2\right) + \delta_-^{(k)}\right). \tag{15b}$$

And finally, the envelope – by analogy with eq. (8) – is given by

$$I_{mix}(u) = E_0^2 \cdot \Phi_0 \cdot \sqrt{g^2(u) + h^2(u)}. \tag{16}$$

For a density wave propagating in a *plane* layer with a *Gaussian* profile, the results from eqs. (15a) and (15b) reduce to those from eq. (9), which was obtained from the more rigorous treatment /8/,/10/ (see Appendix 1).

◇◇◇

In this context we note that the effect of finite lateral thickness on EM scattering in plasmas – i e. *Bragg* scattering from monochromatic waves – was already investigated rather early, e.g. experimentally in 1973 by *Tsukishima et al.* /16/, i. e. 3 years before the first microwave (*E. Mazzucato*) and CO_2 laser (*C.M. Surko* and *R.E. Slusher*) scattering results from a *tokamak* plasma were published (referenced in /2/). See Appendix 3.

Two counter-propagating waves:

We adjust the phases in eq. (12) to the description of FFS from a mode of frequency Ω within an annular layer of thickness L, in a poloidal plane the cross-section of which has the form of (a circle or) an ellipse with axes A^* and B^*, the ratio A^*/B^* being given by the main magnetic field of the *tokamak* or *stellarator*. With U_k, the circumference of a sublayer, and M, the mode number, the associated poloidal wavelength is $\Lambda_k = \frac{U_k}{M}$. $A^* = s \cdot A$ and $B^* = s \cdot B$, where s denotes the size of the center-ellipse referred to a standard case (A, B). The probing beam will intersect this annular layer twice and encounter varying wavelengths Λ_k, in general each of them at different angles $^1\psi_k$ and $^2\psi_k$. Consequently, also the diffraction angles will be different: $^{1,2}\alpha_k$. The normalized wave numbers ^1v_k and ^2v_k will have opposite signs.

In writing down the phases $^{1,2}\delta_\pm^{(k)}$ one must take into account a phase difference Δ between the waves scattered at intersection 1 and those scattered at intersection 2; this phase difference is related to the center-layer (in approximation):

$$\Delta = \frac{d}{w_0} \cdot \left({}^1v_{k_c} - {}^2v_{k_c} \right) ,$$

and is determined by the diplacement d of the beam from the center.

Thus instead of eq. (13) there are now two sets of partial waves:

$$^{1,2}\left(S_{l,r}\right) = \sum_{k=1}^{N_n} {}^{1,2}\left({}^{thin}S_{l,r}^k \right) \cdot \frac{^{1,2}a_k}{2} \cdot exp\left(+i \cdot {}^{1,2}\,\delta_\pm^{(k)} \right) ,$$

with

$$^{1,2}\left({}^{thin}S_{l,r}^k \right) = \mp E_0 \cdot \Phi_0 \cdot exp\left(-\frac{1}{2}(u \pm^{1,2} v_k)^2 (1 - i \cdot {}^{1,2}\,\varsigma) \right) \cdot exp(\pm i\Omega t) . \qquad (18)$$

(Though this allows for different lateral profiles $^{1,2}a_k$, in general it will be assumed that both profiles have the same shape with $\sum^1 a_k = \sum^2 a_k = 1$.) The phase difference Δ between the EM fields scattered at both intersections of the EM beam with the annular layer is included in $^2\delta_\pm^{(k)}$ (details in Appendix 4).

Eventually, the fields ought to be superimposed and squared by analogy with eq. (5), and, as in eqs. (6) and (14), the beat signal is – in the case of complete coherence (for its definition see below) – :

$$I = E_0^2 \cdot \Phi_0 \cdot \left(g \cdot sin(\Omega t) + h \cdot cos(\Omega t) \right) ;$$

in this case the amplitudes g and h are sums:

$$g(u) = {}^1g(u) + {}^2g(u) , \qquad (21a)$$

$$h(u) = {}^1h(u) + {}^2h(u) , \qquad (21b)$$

where $^{1,2}g$ and $^{1,2}h$ are given by a set of equations identical with eq. (15), except for the superscripts "1" and "2", which appear additionally at v_k, ς and $\delta_\pm^{(k)}$ (see Appendix 4).

14

As regards the numerical aspects, the sums in eqs. (15) and (21) converge rather well; in general $N = 33$ sublayers (see eq. (12a)) are sufficient, $N = 257$ being necessary in exceptional cases.

The waves may have lost some degree of coherence on their way between the two intersections; in order to account for that, we introduce a coherence parameter $\kappa \leq 1$:

For complete coherence ($\kappa = 1.$) the envelope of $I(u)$ is given by $I_{miz}(u)$ in eq. (16). With no coherence at all, the scattered intensity will be the sum of the intensities from both layers: $^{1,2}I_{miz}(u) = \sqrt{(^{1,2}g)^2 + (^{1,2}h)^2}$. So in general one has

$$I_{miz}(u) = E_0^2 \cdot \Phi_0 \cdot p(u) ,$$

with (see eqs. (8) and (16))

$$p(u) = \kappa \cdot \sqrt{(^1g +{}^2g)^2 + (^1h +{}^2h)^2} + (1 - \kappa) \cdot \left(\sqrt{(^1g)^2 + (^1h)^2} + \sqrt{(^2g)^2 + (^2h)^2} \right) . \quad (22)$$

Thus in a curve-fitting procedure, the parameters for one $\mathbf{K}$-space profile to fit are the lateral thickness $\vartheta \equiv \frac{L}{\Lambda}$, the displacement d, the degree of coherence κ, the mode number M, the size s of the center-layer and the relative amplitude $\mathcal{A}$. From M the center-layer wavelength $\Lambda \equiv \Lambda_{k_c} = \frac{U_{k_c}}{M}$ can be deduced, U_{k_c} being the circumference of the center-layer.

Once the best fitting $p(u)$ has been found, the absolute value of the "line-integrated" fluctuation level at this $(\Omega, \mathbf{K})$ can be derived in a straightforward manner:

$$\tilde{n}_e \cdot L = \frac{\eta_{beam}}{\eta_{mix}} \cdot \left\{ \frac{\mathcal{J}_{miz}(u)}{\mathcal{J}_{beam}(u) \cdot m(u)} \right\} \cdot \frac{\mathcal{A}}{r_e \cdot \lambda} , \quad (23)$$

where $\{\ \}$ means the average over u; but for a good fit this quotient should be rather independent of u. $\mathcal{J}_{miz}$ and $\mathcal{J}_{beam}$ denote the detector output (in mV) due to the beat power I_{miz} at frequency Ω and the probe beam power I_{beam} respectively (in mW), η_{mix} and η_{beam} the corresponding sensitivities (for example, in mV/mW), and $m(u)$ the "mixing efficiency",

$$m(u) = exp(+u^2) \cdot p(u).$$

4. Results

The CO_2 laser with *Gaussian* beam shape deposited a power of about $10W$ in the plasma; the optics was characterized by $z_0 = -192\,cm$, $w_0 = 0.135\,cm$ and $f = 767\,cm$ (see **Fig.1** and **Fig.5**). The detector system was a linear array of 9 photoconductive Hg:Cd detectors followed by a 9 times 8 frequency channel electronic filter bank (with $\frac{\Delta F}{F} \approx 0.1$, see **Fig.6**).
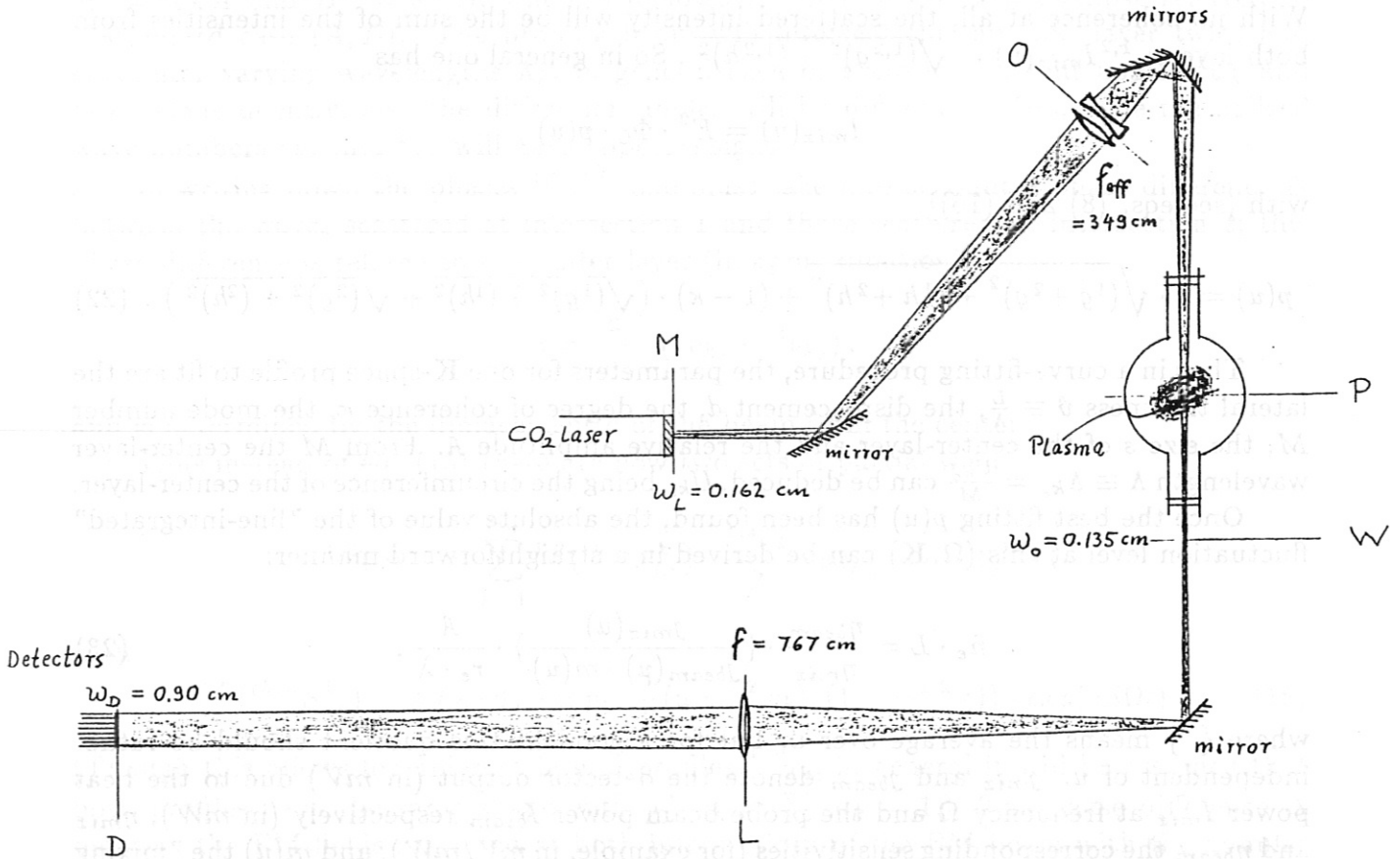

Fig.5 *FFS set-up at the WVII-A; vertical plane, axis of the torus to the right.*
Distances:
    from the coupling mirror M at the laser output to the focussing optics O: 735 cm,
    from the focussing optics O to the beam waist w_0 at W: 615 cm,
    from the beam waist at W to the Fourier lens at L: 767 cm,
    from the Fourier lens at L to the detector plane at D: 767 ,
    from the plasma center at P to the beam waist at W: 192 cm.

16
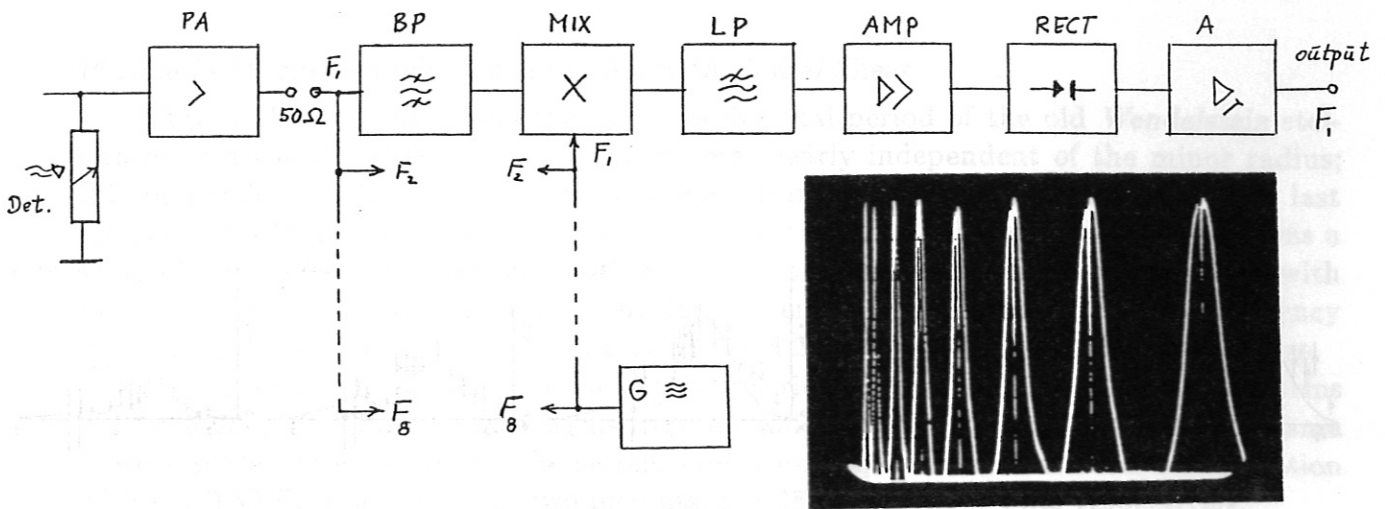
Fig. 6 *The frequency selection for each detector is done by a set of 8 active filter channels in the range from 67 to 900 kHz; this is shown for one channel here: After preamplification, the signal around F is preselected by a passive bandpass filter BP. Then the content of this frequency channel is transformed to low frequencies $\frac{\Delta F}{2}$ ($\leq 50\,kHz$) by mixing it with the center frequency $F = F_1, \ldots, F_8$. The result is passed through a lowpass filter LP to operational amplifiers and is rectified, linearly within 3 orders of magnitude.*

The oscillogramm shows the bandpass transmission profiles, the linear output versus frequency (67, 90, 140, 200, 306, 440, 630, 900 kHz).

Equation (22) was taken to fit the data. The values of Λ_k and ψ_k in eqs. (12) and (13) were derived from the elliptical configuration: poloidally periodic density structures with wave fronts oriented towards the center of the ellipse (and a given radial distribution of amplitudes) are irradiated by an EM beam that passes slightly off axis. The layer was assumed to exist around an elliptical flux surface with $A = 9.\,cm$ and $B = 5.\,cm$ in the standard case (size $s = 1$ for the elliptical center-layer).

For the fits presented here, the lateral, i.e. radial profile of the density structures was taken as *Gaussian*. But the fit result does not depend critically on the particular shape of the radial amplitude profile, and could even be a multiply humped one (as in **Fig. 13**).

With our detector array we encountered some trouble. Eventually, of the original 9 detectors only 5 were still left in the array. In the following we present some data from experimental series with two different types of *W VII-A* plasmas. While the data from the type *"without shear"* were taken with 8 detectors, the data from the type *"with shear"* were obtained with only 5. Since more than 5 u-values were required in these later series, the profiles had to be constructed on a "shot-to-shot" basis from a series of reproducible discharges. We start with these data:
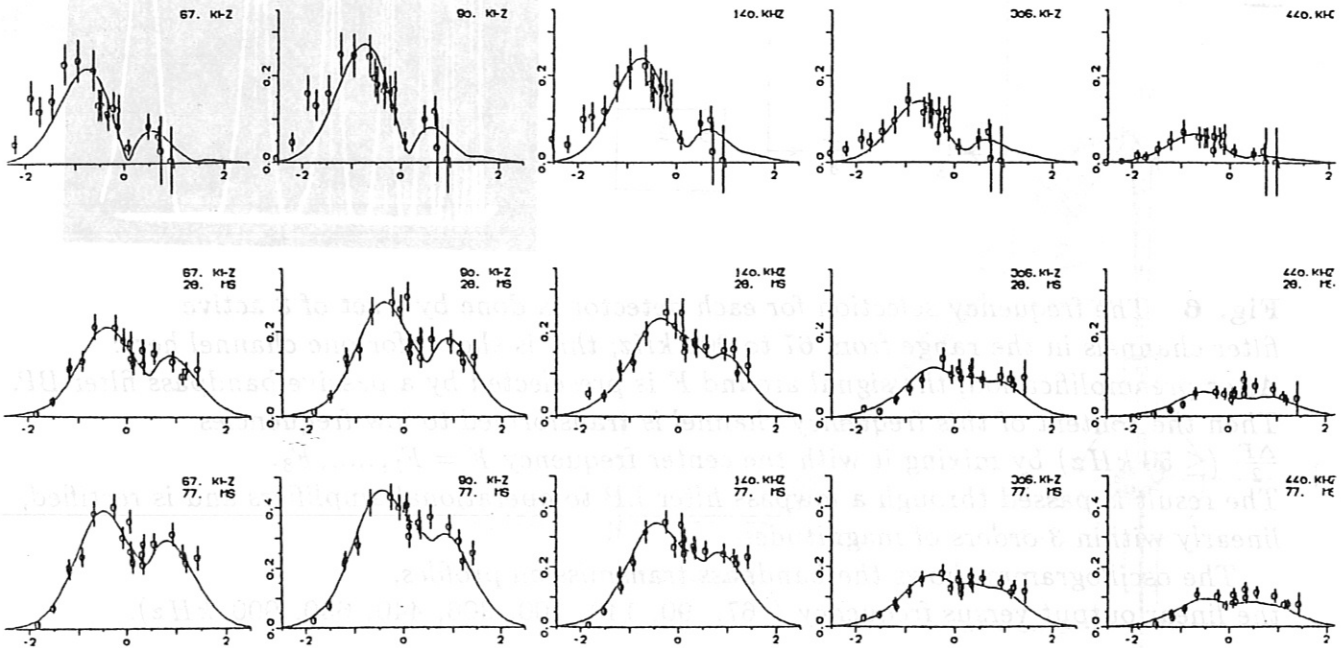
17

Fig. 7 :

FFS data from the W VII-A ECH-heated plasma in sheared field geometry (2.5 T)
for two different series, and best fit curves.
Within one row: the u-distribution (K-space profile) measured at five different
frequency channels and the curves from a least squares fit.

Above: A plasma with central $\iota = 0.44$ at $t = 28\ ms$, fit done with $M = 11;\ d = -1.44\ cm$,
Middle: A plasma with central $\iota = 0.50$ at $t = 28\ ms$, fit done with $M = 9;\ d = +1.38\ cm$.
Below: and at $t = 77\ ms$, fit done with $M = 9;\ d = +1.30\ cm$.

A set of five detectors was used successively
in four different positions across the EM beam waist
during a series of 15 reproducible discharges.
The result is displayed in the "light" of five frequencies.
Abscissa: normalized position u. Ordinate: intensity I_{mix} in arb. units.

The associated parameters ϑ, κ, s and $\mathcal{A}$ are displayed in **Fig. 8** *and* **Fig. 9.**

18

Plasma in Magnetic Field Configuration with Radial Shear

Fig. 7 shows results from the last experimental period of the old *Wendelstein* stellarator. Its rotational transform t is in general nearly independent of the minor radius; this magnetic field is referred as shearless. But the field configuration for these last series of *W VII-A* was exceptional: in contrast to the standard configuration, there was a shear of 5 to 10 % ("*torsatron* operation" /17/); the rotational transform increased with radius. The plasma was maintained by RF power (at the electron cyclotron frequency $\frac{\omega_{ce}}{2\pi} = 70\,GHz$, – "ECH" – , main magnetic field $2.5\,T$), deposited in the plasma core.

Fig. 7 exhibits profiles from two different series with different rotational transforms t. The first horizontal sequence stems from a configuration with $t = 0.44$ (in the plasma center) at the time $t = 28\,ms$, the second and third sequence from another configuration with $t = 0.50$ (in the center) at two instants, $t = 28\,ms$ and $t = 77\,ms$ respectively.

The **K**-space profiles within each row stay remarkably constant in shape, except for the height. This visual impression is confirmed by the outcome of the fit procedure: The best fit is attained with one center-layer wavelength Λ_c common to all frequency channels. This will be outlined in some detail:

The radial position of the plasma layer determines the associated mode number; hence the size s and the mode number M are linked by Λ_c. The least squares fit procedure /18/ was applied in the following way: At first all fit parameters except for the mode number M were varied for each frequency of one series (one row in **Fig. 7**) with different mode numbers; from that the most likely diplacement d was derived and the whole procedure was repeated with d fixed at that value.

The $t = 0.44$ configuration:

This procedure delivered the dependence of the thickness ϑ and the coherence κ on frequency, as shown in **Fig. 8a**. This was done with data from the "*torsatron*" configuration with central $t = 0.44$ at $t = 28\,ms$; $d = -1.44\,cm$ (first sequence in **Fig. 7**). In a third run, in addition to d, the thickness ϑ and the coherence κ were fixed at the values of **Fig. 8a** and the remaining parameters, i. e. center-layer size s and relative amplitude $\mathcal{A}$, were obtained by best fitting to the results from this configuration. As an example, s is plotted versus frequency F for the mode numbers 9 and 11 in **Fig. 8b** ; there is a clear grouping of mode numbers: at all frequencies (except of the last one at ($0.44\,MHz$, but compare **Fig. 7**), a mode number 11 would originate from the same layer: $s = 1.15$; the mode number 9 would stem from another layer further inside, etc. Layers $d < 1.2$ can be ruled out because they would exist outside the limiter.

The plasma carried a toroidal electric current (up to $1\,kA$, created externally by a slight asymmetry in the ECH irradiation and driven internally by neoclassical diffusion in the toroidal magnetic field configuration); this current enhanced the positive shear of t, as a result of which a magnetic flux surface of the rotational transform $t = 5/11 = 0.4545...$ may be expected near the plasma edge. The standing-wave pattern with $M = 11$ reminds one that the magnetic field configuration at this "rational" surface tends to develop "islands" of poloidal periodicity 11 when some disturbance is active.

The amplitude distribution versus frequency for this configuration, $M = 11$, $s = 1.15$ and $d = -1.44\,cm$ is shown in **Fig. 8c**.
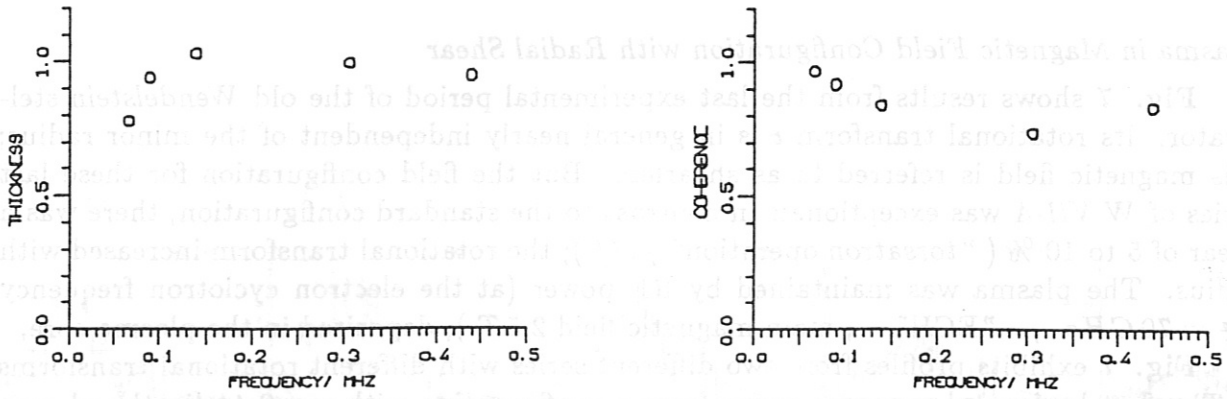
Fig. 8a: *Thickness ϑ and coherence κ versus frequency, for the $t = 0.44$ configuration.*
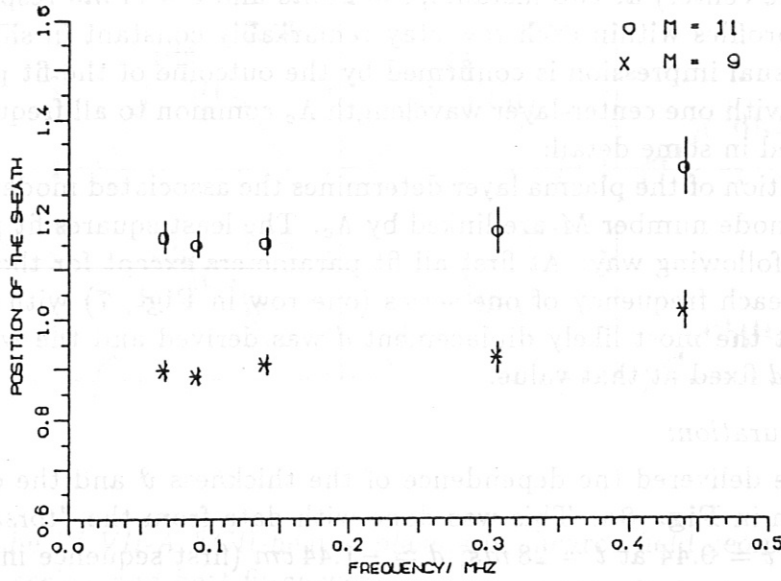

Fig. 8b: *The size s of the center-layers with mode numbers 9 and 11 versus frequency, for the $t = 0.44$ configuration, with $d = -1.44$ cm.*
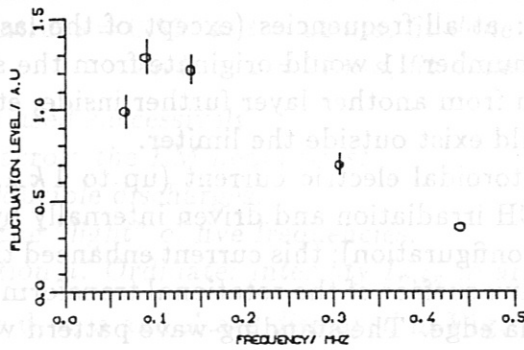

Fig. 8c: *Relative amplitudes A versus frequency for the $t = 0.44$ configuration of the $M = 11$ mode in the $s = 1.15$ layer*

The t = 0.50 configuration:

Comparison of the middle and lower rows in **Fig. 7** for the $t = 0.50$ configuration shows that there is very little dependence on time. At both instants, with slightly different displacements d, the K-space profiles can be well fitted with a mode number $M = 9$ at all five frequencies (**Fig. 9c**, which was obtained with ϑ and κ from **Fig. 9a**), though not as convincingly as in the other configuration. In this dicharge, $t = 5/9 = 0.555...$ might be attained at the plasma edge. Does **Fig. 9c** indicate different positions s of the $M = 9$ layer at different instants of time t?

The relative amplitude A versus frequency is diplayed in **Fig. 9b**, for $t = 28\,ms$ and for $t = 77\,ms$; it reveals a frequency band with a maximum at $F \approx 100\,kHz$, and a high frequency roll-off of $\frac{\Delta\omega}{\omega} \approx 1.$ at $77\,ms$ and of $\frac{\Delta\omega}{\omega} \approx 1.5$ at $28\,ms$.

The error bars represent standard deviations, i.e. with a probability of 67 % the best estimate of the fit parameter will be found within that range.
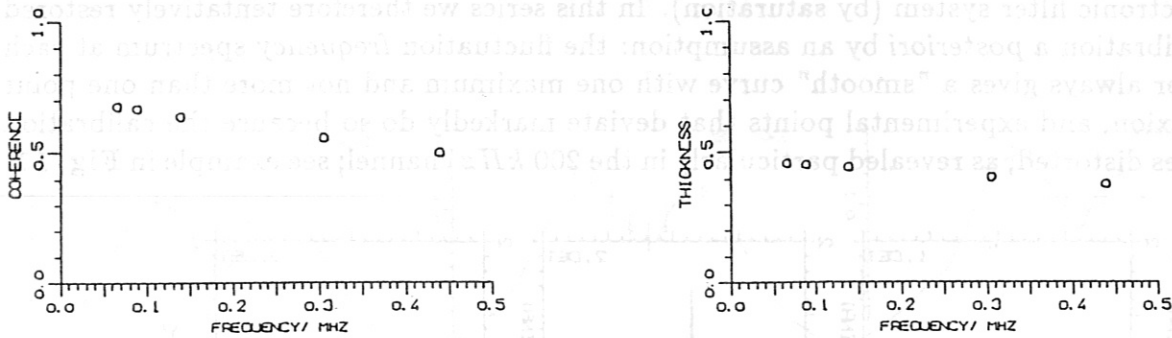
Fig. 9a: *Coherence κ and thickness ϑ versus frequency F for the series with $t = 0.50$, both at $t = 77\,ms$ and at $t = 28\,ms$.*
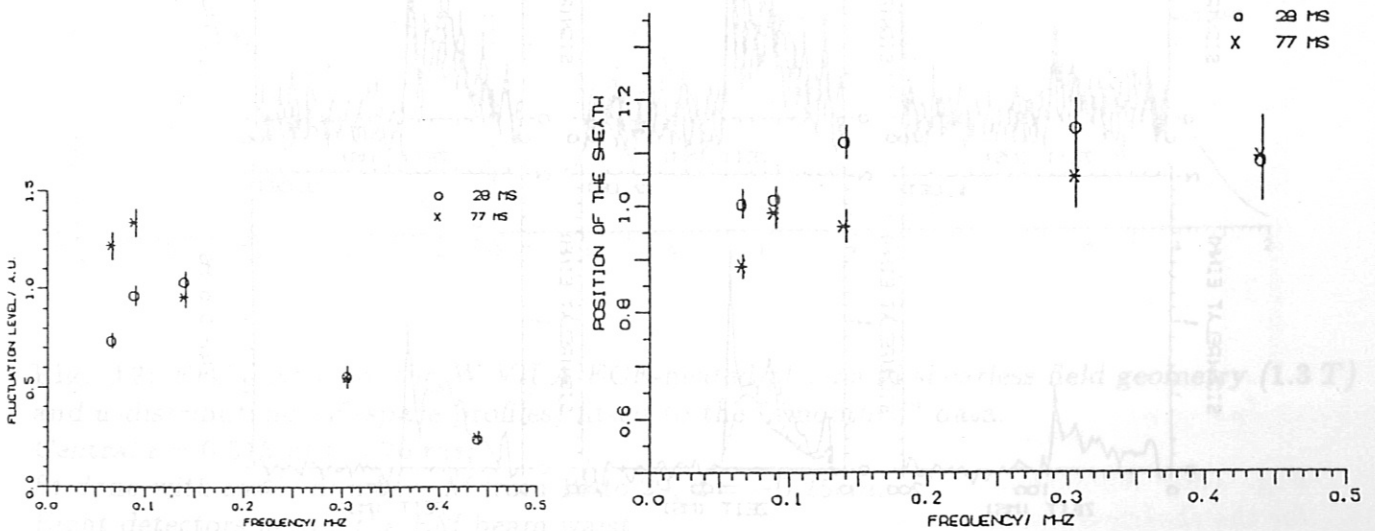

Fig. 9b: *Amplitude A versus frequency for the same series (as in Fig. 9a).*

Fig. 9c: *The size s of the center-layer with mode number 9 versus frequency for $t = 0.50$ at the times $t = 28\,ms$ and $t = 77\,ms$.*

21

Plasma in Shearless Magnetic Field Configuration

   This is a series run prior to that discussed in **Fig. 7**; the array was then still (nearly) in order, and the 8 different *u*-values stem from 8 different detectors (**Fig.12**).

   The plasma was again maintained by ECH deposition, this time at $2 \cdot \frac{\omega_{ce}}{2\pi} = 70\,GHz$, 6 *cm* outside the magnetic axis, and the magnetic configuration was standard, i.e. nearly shearless, with central $\iota = 0.515$. The main magnetic field was 1.3 *T*.

   Fig. 10 contains raw data of the points to fit in **Fig. 12**: the time response $\jmath(t)$ (voltage versus time, see eq.(23)) of the detector-amplifier system for three detectors (i.e. three different values of *u*) at a selected frequency (140 *kHz*); in the first sequence the superimpositioning of five reproducible discharges, in the second their mean, averaged in a 3 *ms* time interval. The noise was not created by the shot noise of the beam power, as it should be with a good detector system, but rather by electromagnetic pick-up noise of unknown origin. This noise was sometimes strong enough to spoil the calibration system of the electronic filter system (by saturation). In this series we therefore tentatively restored the calibration *a posteriori* by an assumption: the fluctuation *frequency* spectrum at each detector always gives a "smooth" curve with one maximum and not more than one point of inflexion, and experimental points that deviate markedly do so because the calibration becomes distorted, as revealed particularly in the 200 *kHz* channel; see example in **Fig. 11**.
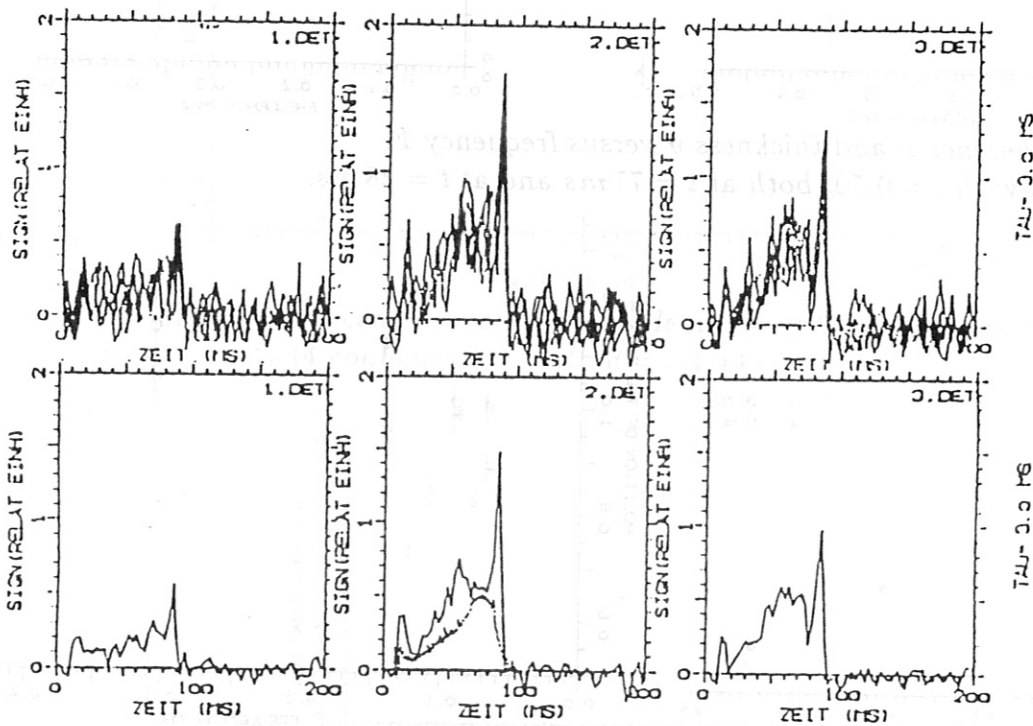

Fig. 10: *An example of the raw data from three detectors at 140 kHz: the response of three detectors versus time.*

above: the traces of five reproducible discharges
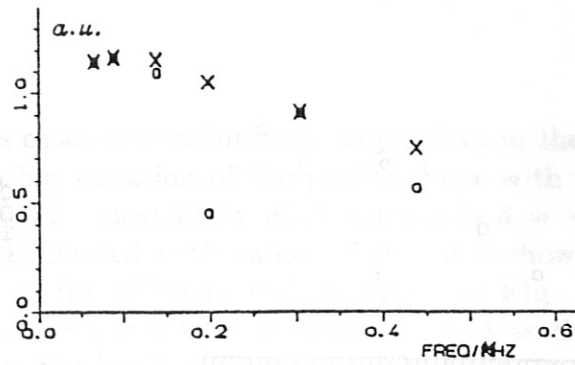*below: averaged in a 3 ms time interval.*

The central box below contains the line density for comparison (lower trace).
The evaluation of these data is shown in **Fig. 12**.

Fig. 11: *The frequency distribution in one detector.*
Circles: original
Crosses: "smoothed"
as described in the text

The error bars in **Fig. 12** were roughly estimated from the data in **Fig. 10**. Because of the smoothing procedure they are somewhat arbitrary; but these uncertainties do not sensitively affect the variances of the fit parameters in **Fig. 13**.
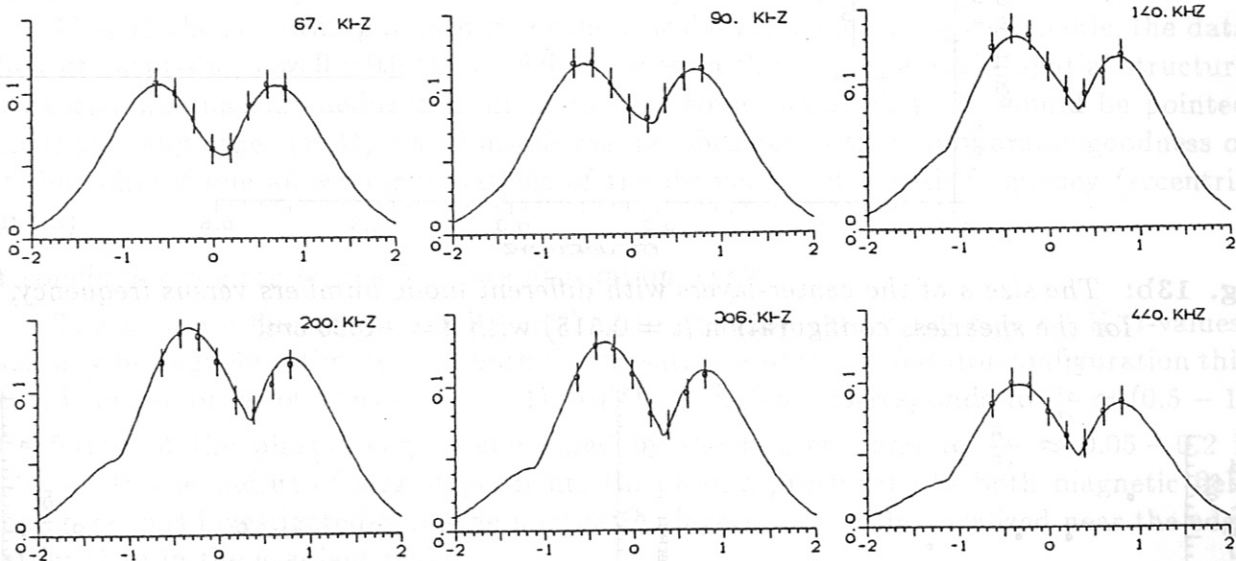

Fig. 12: *FFS data from the W VII-A ECE-heated plasma in shearless field geometry (1.3 T) and u-distributions (K-space profiles) fitted to the "smoothed" data.*
Central $\iota = 0.515$ at $t = 70$ ms;
fit done with mode numbers M from 19 to 29, $d = -0.25$cm.
Eight detectors across the EM beam waist
measure the beat signal in the "light" of six frequencies.
Abscissa: normalized position u. Ordinate: intensity I_{mix} in arb. units.

The associated parameters ϑ, κ, s, A and M are displayed in **Fig. 13**.
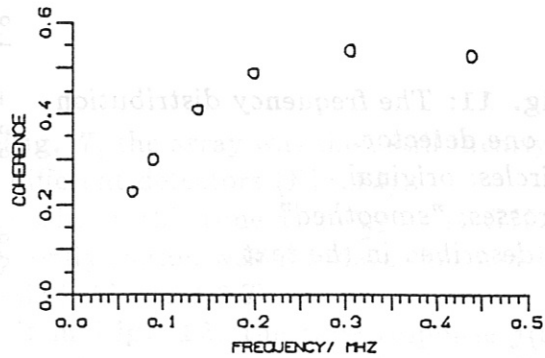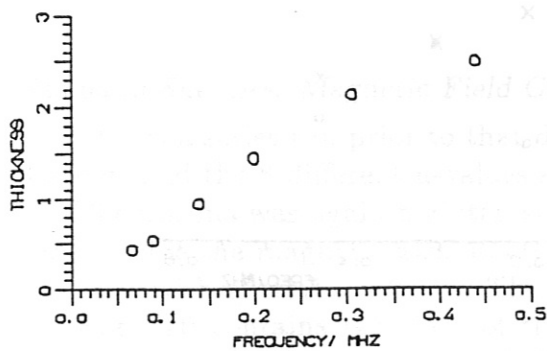
Fig. 13a: *Thickness ϑ and coherence κ versus frequency, for the shearless configuration.*
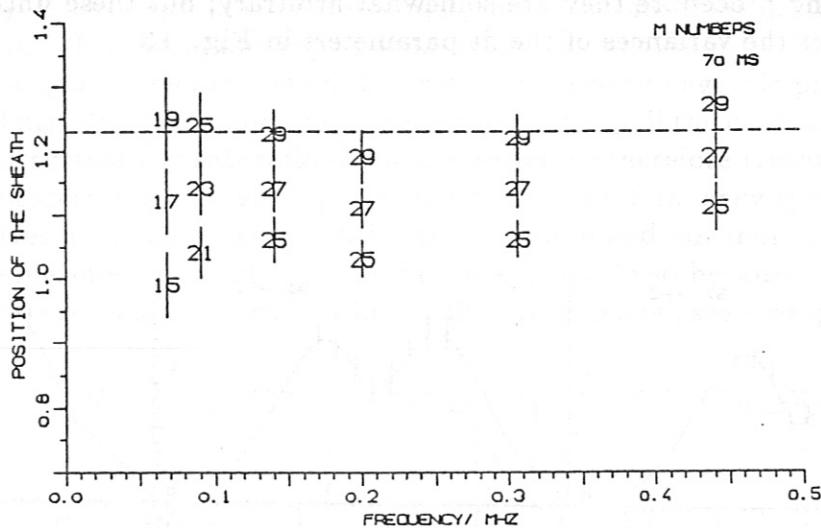

Fig. 13b: *The size s of the center-layers with different mode numbers versus frequency, for the shearless configuration ($t = 0.515$) with $d = -0.25$ cm.*
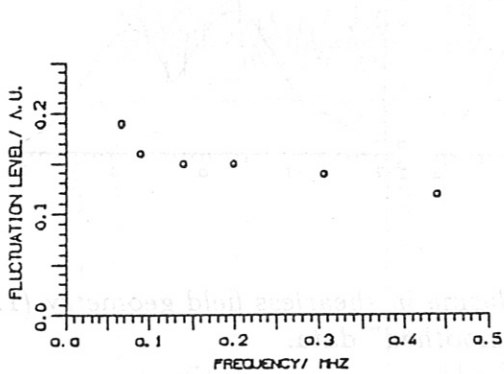

Fig. 13c: *Amplitudes A versus frequency for the shearless configuration in the $s = 1.23$ layer with mode numbers shown in **Fig. 13d**.*
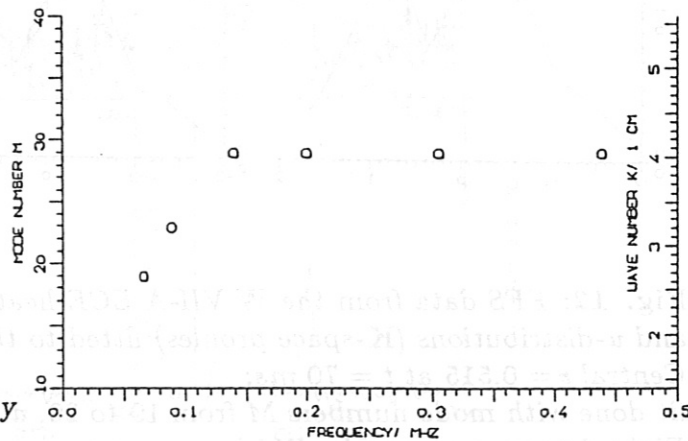
Fig. 13d: *Mode number M versus frequency ("dispersion") in the $s = 1.23$ layer of the shearless config.; $t = 70$ ms; $d = -0.25$ cm.*

24

The wave numbers in this shearless case are considerably larger than in the previous one with shear. In **Fig.12**, there is no big variation of the profile shape with frequency either, except at 67 kHz and 90 kHz. The most likely displacement is $d = -0.25\ cm$. When the size s of the center-layer is evaluated with values of ϑ and κ shown in **Fig. 13a** and plotted versus channel frequency for different mode numbers in **Fig. 13b**, one is led to choose a grouping of mode numbers in a layer around $s = 1.23$ as the best fit to the data (**Fig. 13d**); the slope $\frac{d\Omega}{d\mathbf{K}}$ at the low-frequency channels results in a velocity of $\approx 2.2\ \frac{km}{sec}$. On the one hand, this value is comparable to that of the velocity with which the plasma rotates poloidally (as we know from the *Doppler* shift of impurity line radiation); on the other hand, it is also of the order of the phase velocity that drift waves would have with these wave numbers. (In CGS units this velocity is given by $w_{perp} = ckT/eBr_n$; $\frac{1}{r_n} \equiv \frac{d}{dr}(ln\, n_e)$, — and with $kT = 1.6 \cdot 10^{-10}\ erg$ ($T_e \approx 100\,eV$), $B = 1.3 \cdot 10^4\,Gauss$ and $r_n = 5\,cm$ one gets the result: $w_{perp} \approx 1.5\ \frac{km}{sec}$.) The wave number $M = 29$ in the plateau of **Fig. 13d** corresponds to $\mathbf{K} \cdot \rho_i \approx 0.4$, when an ion gyro radius of $\approx 0.1\ cm$ is chosen ($T_e \approx 50\ eV$). In this magnetic configuration, a flux surface with $\iota = 15/29 \approx 0.517$ may be expected to exist near the plasma edge. The associated relative amplitudes versus frequency are presented in **Fig. 13c**.

Though the smoothing procedure of the raw data is somewhat questionable, the data then fit surprisingly well with the model assumed in this paper, and the spatial structure of density fluctuations deduced from them bear some plausibility. It should be pointed out that many other ($\mathbf{K}$,Ω)-distributions can be obtained with a comparable goodness of fit, but only if one allows for variations of the displacement d with frequency (eccentric layers).

A concluding remark on the absolute fluctuation level:

The absolute fluctuation level according to eq. (23), integrated over all $\mathbf{K}$,Ω-values, can only be vaguely estimated. In both the *torsatron* and the *stellarator* configuration this level is of the order of $^{tot}\tilde{n}_e \approx (0.5 - 1) \cdot 10^{12}\ cm^{-3}$. This corresponds to $\frac{\tilde{n}_e}{n_e} \approx (0.5 - 1)$ if referred to the plasma edge (determined by the limiter), and to $\frac{\tilde{n}_e}{n_e} \approx 0.05 - 0.2$ if referred to the radius of largest gradients (in plasma pressure). In both magnetic field configurations investigated here, the fluctuation layers seem to be localized near the edge rather than in the gradient region.

25

5. Discussion

In the past, a previous CO_2 laser scattering device at $WVII - A$ /4/ was designed for FS with an external LO. The probing beam itself, having traversed the fluctuating plasma, was attenuated and used as LO (in *homodyning*). It turned out that the LO was thus "loaded" with information on small-angle forward scattering from long-wavelength fluctuations (order of cm), which had been erroneously attributed to short wavelengths (order of mm). Results obtained with a LO that by-passed the plasma indicated that these fluctuations in the cm scale exceed that in the mm scale. We therefore modified our FS system into a FFS system, instead of choosing the more reasonable approach, a hybrid system, likewise suitable for performing FS and FFS, as somewhat later has been done at the $TEXTOR$ tokamak /19/. Because of this deficiency the data from 10 μm are not directly comparable with those from microwave scattering /3/, that was done from mm density wavelengths. As already mentioned before, we presume that mm fluctuations prevail in the bulk plasma and cm fluctuations at the edge.

We do not claim that the spatial distribution of fluctuations assumed here is the only one which results in the kind of scattering signals observed; but at least the separation of the maxima of the K-space profiles hints at wavelengths of $2 - 4$ cm; and the essential point is that the asymmetry can only be explained by anisotropy of the fluctuations. Other models are conceivable since this one is not comprehensive either ; for instance, the case of a spread also in mode number (for one Ω) has not been treated here; this may be necessary to postulate in order to account for the observed Ω spread.

The model presented here corresponds to a particular *Schlieren* effect, created by the counter-propagation of two almost identical density waves with extended and nonparallel fronts. The degree of asymmetry of the resulting scattering profile can be controlled by – among other means – the amplitude ratio of the fields scattered from the two counter-propagating waves. The $WVII - A$ plasma cross-section is elliptical in shape, and the probing beam intersects its axes at an angle of 45^0. Whith finite lateral thickness ϑ, the amplitude ratio of the scattered fields is determined by the amount d of off-axis observation, and it is different from 1. even when a poloidally uniform fluctuation amplitude distribution is assumed; this is because the scattered field amplitudes depend on the angle of irradiation ψ, which is different at the two intersections of the annular layer, ψ_1 and ψ_2 (see Appendix 5). One can also imagine a poloidally non-uniform distribution (top/bottom asymmetry), and in the case of a circular plasma cross-section (like $TOSCA$), where ψ_1 and ψ_2 are equal, this may be the only possible origin of unequal co-/counter-scattering field amplitudes.

But it should be stressed that the picture of structures with non-parallel wave fronts is essential. Moderate asymmetries like those in **Fig. 7** middle/below or that reported from $TOSCA$ /9/ (Fig. 18 there) can be fitted by a simple model of counter-propagating density waves, as has been demonstrated in /12/ (Fig. 4 there), but strong asymmetries like those in **Fig. 7** above cannot be fitted without "spatial dispersion". This is illustrated in **Fig. 14**. Neither thin counter-propagating waves nor ones that are thick but have parallel wave fronts result in appreciable asymmetries.
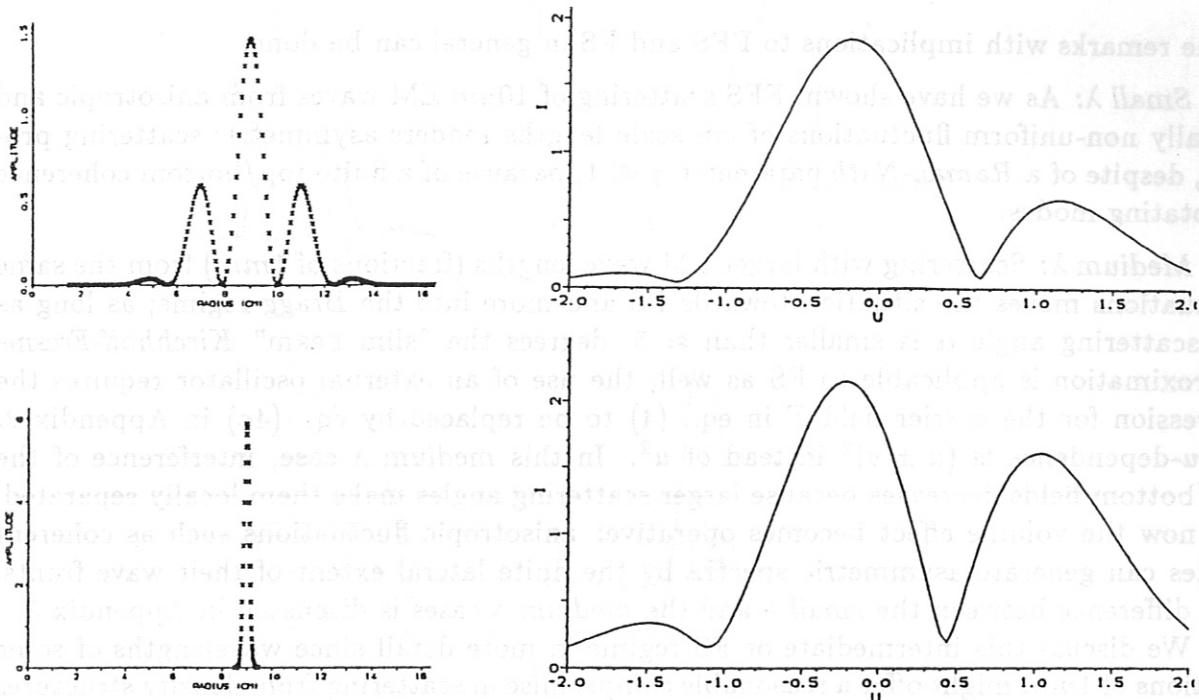
Fig. 14: *The influence of the radial shape of the density profile (left: a_k versus radius) on the shape of the K-space profile (right: beat signal I_{mix} versus detector location u) for FFS from poloidal fluctuations in an elliptical layer the axes of which are intersected by the EM beam at 45^0.*
In this example $A = 9$ cm, $B = 5$ cm, $d = 1.05$ cm; $M = 11(\rightarrow \Lambda \approx 4$ cm$)$, $\kappa = 1.0$.

Above: a radially extended "multiple Gaussian" with $\delta = 0.93$.
Below: a practically thin layer with $\delta = 0.05$.

Note the difference in asymmetries.

For the investigation of density fluctuations in the *cm* scale length quite another scattering method might be more appropriate, that has been developed and applied to a *tokamak* plasma by *H. Weisen* /15/. It is a specific form of spatial filtering technique, introduced 1935 by *Zernike* as an essential improvement of microscopy and since then is called the phase contrast method. With this, the information contained in the EM wave front (*Weisen* used a CO_2 laser) acquired by phase fluctuations is not recovered in the far field of the probing beam (as with ordinary scattering) but in the near field, and complicated wave patterns can thus be viewed directly in real space. But unfortunately, the probing beam diameter should be at least equal to the structure size to investigate, and the narrow access to *stellarator* plasmas excludes this phase contrast method.

27

Some remarks with implications to FFS and FS in general can be done:

Small λ: As we have shown, FFS scattering of $10\mu m$ EM waves from anisotropic and radially non-uniform fluctuations of cm scale lengths renders asymmetric scattering profiles, despite of a *Raman-Nath* parameter $\gamma \ll 1$, because of a finite top/bottom coherence of rotating modes.

Medium λ: Scattering with larger EM wave lengths (fractions of $1mm$) from the same fluctuations moves the situation towards FS and more into the *Bragg* regime; as long as the scattering angle α is smaller than ≈ 5. degrees the "slim beam" *Kirchhoff-Fresnel* approximation is applicable to FS as well; the use of an external oscillator requires the expression for the carrier field T in eq. (4) to be replaced by eq. (4a) in Appendix 2: the u-dependence is $(u \pm v)^2$ instead of u^2. In this *medium* λ case, interference of the top/bottom fields decreases because larger scattering angles make them locally separated, but now the volume effect becomes operative: anisotropic fluctuations such as coherent modes can generate asymmetric spectra by the finite lateral extent of their wave fronts. The difference between the *small* λ and the *medium* λ cases is discussed in Appendix 5.

We discuss this intermediate or FS regime in more detail since wavelengths of some fractions of $1mm$ might offer a reasonable compromise in scattering from density structures in the cm region, at least when the access to the plasma is restricted:

In this situation, at larger values of K ($\geq\approx 10.$ cm^{-1}) deviations from isotropy such as periodic fluctuations with extended wave fronts, will definitely create a volume effect, and the width of the **K** and Ω spectra can serve as an indicator: these fluctuations will yield narrow spectra; observation of broad spectra will probably rule out anisotropy.

At smaller values of **K** ($\leq\approx 8.$ cm^{-1}), this indicator can not be quite as helpful. Commonly used beam widths w_0 then represent values of $v = Kw_0$ too small to give a sufficient K-resolution (see Appendix 2).

But even at larger values of **K**, i.e. with a "K-apparatus profile" sufficiently narrow, anisotropic fluctuations can yield broad K-spectra; this is illustrated at an example in **Fig. 15 b** with $|\mathbf{K}| \approx 8.$ cm^{-1}. There we demonstrate three criteria, useful in asking for the degree of isotropy: In addition to

1) the width of the **K**,Ω spectra

two other features are of importance:

2) the dependence on the angle of irradiation ψ and
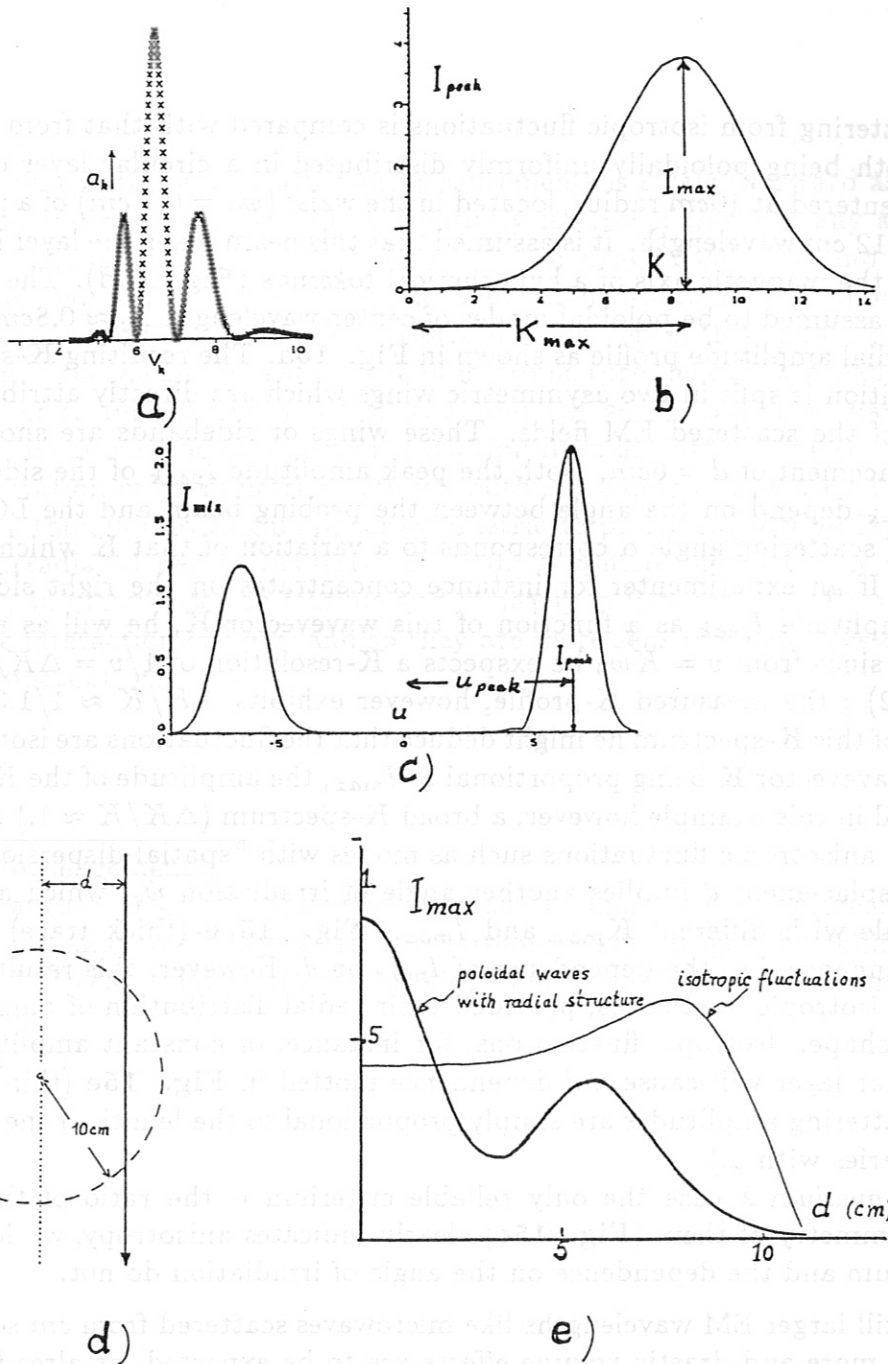
3) the ratio of amplitudes of the sidebands.

Fig. 15: *An example: Scattering of $\lambda = 0.012$ cm waves in a beam with $w_0 = 0.7$ cm by poloidal modes of center-wavelength $\Lambda_c \approx 0.8$ cm at $r = 10$ cm and by isotrop. flucts. The radial profile a) of the fluctuation amplitudes is a "Multigaussian" with $L = 4$ cm. The right sideband peak, I_{peak} in c), is plotted versus $\mathbf{K}$, which corresponds to different angles between the probing beam and the LO, in b). This fluctuation structure is probed by the EM beam at various displacements d, see d). c) and b) have been calculated with a diplacement of $d = 6$ cm. In e) the maximum of the $\mathbf{K}$-distribution, I_{maz}, is plotted versus the displacement d (thick trace) and for comparison the result for scattering from isotropic fluctuations in the same sheath is indicated (thin trace)*

29

In **Fig. 15** scattering from isotropic fluctuations is compared with that from anisotropic fluctuations, both being poloidally uniformly distributed in a circular layer of thickness $L = 4\,cm$ and centered at $10cm$ radius, located in the waist ($w_0 = 0.7\,cm$) of a probing EM beam of $\lambda = 0.012\,cm$ wavelength. It is assumed that this beam scans the layer in a varying distance d from the magnetic axis of a hypothetical *tokamak* (**Fig. 15d**). The anisotropic fluctuations are assumed to be poloidal modes of center-wavelength $\Lambda_c \approx 0.8cm$ (thickness $\vartheta = 5$) and a radial amplitude profile as shown in **Fig. 15a**. The resulting K-*space* profile under this condition is split in two asymmetric wings which are directly attributed to the two sidebands of the scattered EM fields. These wings or sidebands are shown in **Fig. 15c**, for a displacement of $d = 6cm$. Both the peak amplitude I_{peak} of the sidebands and its position u_{peak} depend on the angle between the probing beam and the LO beam. A variation of this scattering angle α corresponds to a variation of that **K** which dominates the scattering. If an experimenter for instance concentrates on the right sideband and measures its amplitude I_{peak} as a function of this wavevector **K**, he will as a result get **Fig. 15b**, and, since from $v = Kw_0$ he exspects a K-resolution of $1/v = \Delta K / K \approx 1/5.5$ (see Appendix 2) ; the measured K-profile, however exhibits $\Delta K / K \approx 1/1.3$, therefore from the width of this K-spectrum he might deduce that the fluctuations are isotropic, their amplitudes at wavevector **K** being proportional to I_{max}, the amplitude of the K-spectrum. As demonstrated in this example however, a broad K-spectrum ($\Delta K / K \approx 1.$) may as well be generated by anisotropic fluctuations such as modes with "spatial dispersion".

Another displacement d implies another angle of irradiation ψ_c, which again yields another **K**-profile with different $\mathbf{K}_{max}$ and I_{max}. **Fig. 15 e** (thick trace) shows this directional dependence, i.e. the dependence of I_{max} on d. However, this result could also be produced by isotropic fluctuatios, provided their radial distribution of amplitudes has the appropiate shape. Isotropic fluctuations, for instance, of constant amplitude in this $4cm$ wide circular layer will cause a d dependence plotted in **Fig. 15e** (thin trace; – in this case the scattering amplitudes are simply proportional to the length of the interaction region, which varies with d.)

So in this *medium* λ case the only reliable criterium is the ratio of the sideband amplitudes; asymmetry of them (**Fig. 15c**) clearly indicates anisotropy, while the width of the K-spectrum and the dependence on the angle of irradiation do not.

Large λ: Still larger EM wavelengths like microwaves scattered from cm scale lengths enhances γ still more and drastic volume effects are to be expected, as already has been pointed out by *v.Hellermann* /8/. In addition, at these wavelengths gross refraction must be accounted for. Precautions to avoid undue explanation of the results is more urgent. In the $2mm$ scattering design at $WVII - A$ /3/ observation of both sidebands was technically not possible.

Résumé:

The interpretation of scattering measurements is straightforward as long as the fluctuations in the scattering volume are entirely isotropic; then for any scattering angle α there will always be components that match the *Bragg* condition, and the local spectral density derived will not depend on the angle of irradiation ψ. Although it is common use to judge: broad spectra indicate isotropic turbulence, this should be done with some reluctance. Truely, a significant feature of isotropic turbulence is a broad spectrum in both wavenumber K and frequency Ω ($\frac{\Delta\Omega}{\Omega} \approx 1.$ and $\frac{\Delta K}{K} \approx 1.$). But as we have shown, a broad K-spectrum can also be obtained in scattering from anisotropic fluctuations.

Observation of asymmetries between both sidebands will at least be an indication of anisotropy, though they might appear symmetric despite of anisotropic layers if accidentally they are irradiated perpendicularly: $\psi_c = 0$. A control measurement of both sidebands in FS may in many cases be feasible and is nearly indispensable. FFS schemes inevitably detect the interaction of both, and so they are more sensitive detectors of deviations from isotropic fluctuations.

31

Appendix.

A1.

For a density wave propagating in a *plane* layer the wavelength within the layer is constant: Λ_k is identical with Λ_c. With the subscript "c" omitted, v_k is identical with v, eq. (13) reduces to

$$^{plane}S_{l,r} = {}^{thin}S_{l,r} \cdot \sum_{k=1}^{N_n} \frac{a_k}{2} \cdot exp(+i\delta_\pm^{(k)}),$$

with $\delta_\pm^{(k)} = \pm(k-k_c) \cdot {}^{Bragg}\delta_\pm$; and eqs. (15) reduce to

$$^{plane}g \cdot exp(+\frac{1}{4}v^2) = exp\left(-(u-\frac{v}{2})^2\right) \cdot \sum_{k=1}^{N_n} a_k \cdot sin(\epsilon_+ + \delta_+^{(k)})$$

$$+ exp\left(-(u+\frac{v}{2})^2\right) \cdot \sum_{k=1}^{N_n} a_k \cdot sin(\epsilon_- + \delta_-^{(k)}), \qquad (17a)$$

$$^{plane}h \cdot exp(+\frac{1}{4}v^2) = exp\left(-(u-\frac{v}{2})^2\right) \cdot \sum_{k=1}^{N_n} a_k \cdot cos(\epsilon_+ + \delta_+^{(k)})$$

$$- exp\left(-(u+\frac{v}{2})^2\right) \cdot \sum_{k=1}^{N_n} a_k \cdot cos(\epsilon_- + \delta_-^{(k)}). \qquad (17b)$$

Any distribution may be chosen for the amplitudes a_k; with a *Gaussian*, eqs. (17) give the same result as eq. (9).

And in particular, for a triangular distribution with $n = 0$ ($N = 3$; $k = -1, 0, +1$; $a_{-1} = 0$, $a_0 = 1$, $a_{+1} = 0$), equations (17a) and (17b) lead to the description of a thin layer, like eqs. (7).

A2.

It is instructive to consider the effect of finite lateral thickness of a density wave in terms of *Fourier* transform: A laterally infinitely extended plane wave is characterized by a single K, i.e. the spatial spectrum $S(K)$ of a density wave with large lateral extent is narrow, scattering will occur constructively only near the "*Bragg* condition" (see below). On the other hand, a laterally "thin wave" - asymptotically approximated by a plane phase screen as in eqs. (1) and (2) - is *Fourier* composed by a broad spectrum $S(\mathbf{K})$, and scattering will therefore occur at nearly any angle of incidence ψ_c (*Raman-Nath* scattering).

From eqs. (7) and (8) follows: the sidebands of ${}^{thin}p(u)$ have their maximum at $u_{max} \approx \pm\frac{v}{2}$, as is shown in the FFS curve (*a*) in **Fig.A1**.

The height of the maximum in FFS is governed by $exp(-\frac{v^2}{4})$ (eq. (8)). For v somewhat larger than 2.5 the "self-mixing" ceases to be efficient and the use of an external LO is advisable (FS); in this case the carrier is:

$$T_{LO} = E_{LO} \cdot exp\left(-\frac{1}{2}(u \pm v)^2(1 - i\varsigma)\right) \qquad (4a)$$

(instead of eq. (4)). Equations analogous to (7) then indicate that in this case the sidebands have their maxima at $u_{max} \approx \pm v$. This is curve (b) in **Fig.A1**. (The ordinates I_{max} of (a) and (b) are different in scaling.)
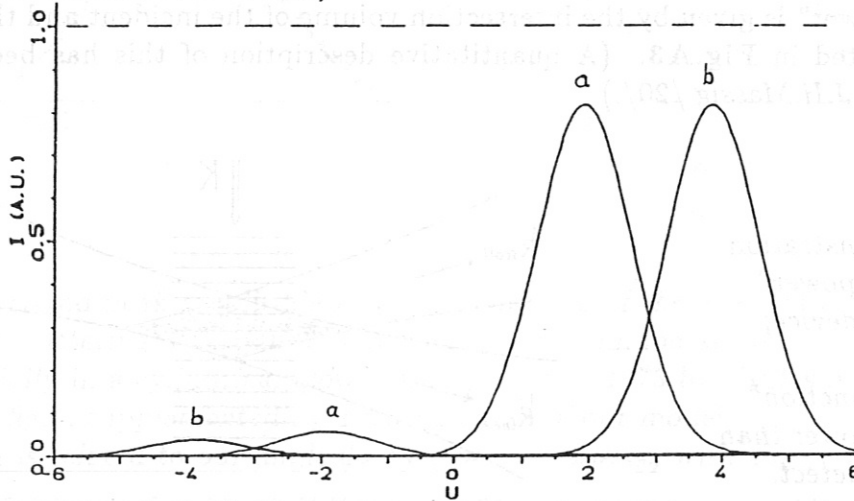

Fig.A1 *The sidebands for $\lambda = 0.875 cm$, $\Lambda_c = 1.8 cm$ and $\psi_c = 25°$, the lateral profile of the density wave front being a s Gaussian with $L = 1.8$ cm. (The Bragg condition for the right sidebands is satisfied with $\psi_{Bragg} = 14°$). $w_0 = 1.$ cm yields $v = 3.85$ ($z_{mi} = 0.$). For $L = 0.$ all sidebands would have $I_{mix} = 1$. (broken line); a): in FFS the absolute value is so small that in practice an external LO will be added: FS, the result of which is shown in b). Then the maximum shifts from $u_{max} \approx \pm\frac{v}{2}$ to $u_{max} \approx \pm v$.*

If we take the sideband maximum I_{max} as a measure of its intensity, then we get its dependence on ψ_c, the angle of irradiation, by evaluating $I_{max} \equiv I_{mix}(u_{max})$ as a function of ψ_c, this dependence being the same for FS and FFS. The result is presented in **Fig.A2**; parameter is the normalized thickness $\vartheta \equiv \frac{L_c}{\Lambda}$. One recognizes the meaning of the condition $^{Bragg}\delta_\pm^{(k)} = 0$ in eq. (12): it determines the angle of maximum sideband intensity in FFS, which reveals the "Bragg condition" $sin\psi_{Bragg} = \pm\frac{1}{2}\frac{\lambda}{\Lambda_c}$.

Fig.A2:
The maximum I_{max} of the right sidebands in Fig.A1 as a function of ψ_c, the angle of irradiation (both for FS and FFS); parameter is the thickness $\vartheta = \frac{1}{2}, 1, 2, 4, 8$. Otherwise parameters as in Fig.A1.
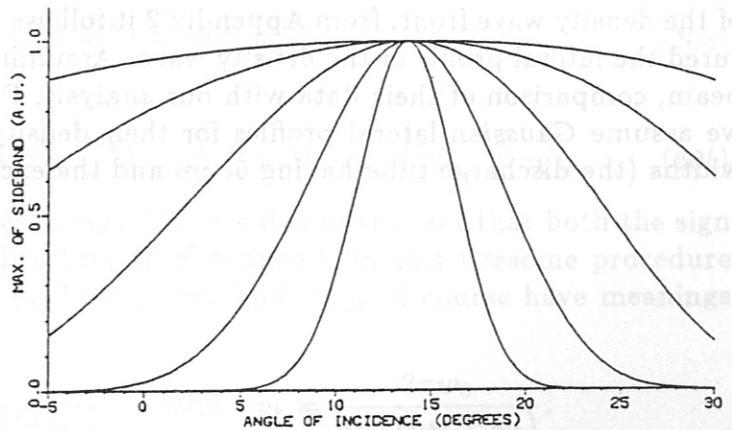
The angular dependence $I_{max}(\psi_c)$ in **Fig.A2** reflects the *Fourier-transform-like* behaviour of the lateral profile of the density wave front: the larger the extension L of the wave front, the narrower is the **K**-spectrum and the more narrowly is the scattered power concentrated around the *Bragg* angle ψ_{Bragg}.

Whether or not a narrow "K-line" can be resolved by a scattering device, depends on its "apparatus function", in complete analogy to ordinary spectroscopy. Qualitatively, the "resolving power" is given by the intersection volume of the incident and the scattered beams, as indicated in **Fig.A3**. (A quantitative description of this has been given by *E.Holzhauer* and *J.H.Massig* /20/.)

Fig.A3:
*Qualitative demonstration
of the "resolving power"
of the scattering device;
in this case
the "apparatus function"
is somewhat narrower than
the spectrum to detect.*
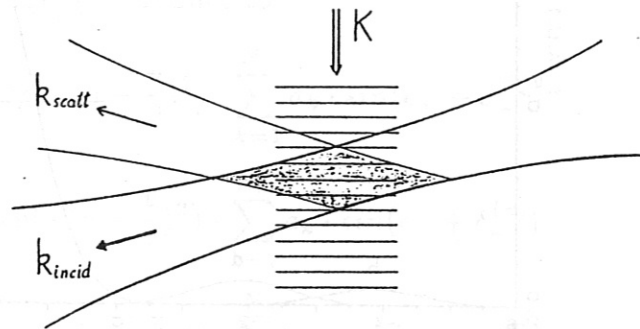
If the lateral extension of the density wave does not "fit" into the intersection volume then the observed **K**-spectrum will be "smeared out" by the poor resolving power, just as in ordinary spectroscopy a $1\mathring{A}$ line would be smeared out by a spectroscope with a $5\mathring{A}$ resolution. (So in case one would like to calibrate the resolution of a scattering device, the waves serving as calibration source should have a lateral extension at least equal to the length of the intersection volume.)

A3.

Tsukishima et al. /16/ scattered 35 GHz microwaves by ion-acoustic waves propagating in a low-density d.c. discharge along the axis of the cylindrical tube, and they measured scattered signals as a function of the angle of irradiation ψ_c, keeping **K** constant. Since the angular dependence, **Fig. A2**, behaves as the *Fourier*-transform of the lateral profile of the density wave front, from Appendix 2 it follows that, by varying ψ_c, the authors measured the lateral profile of the density wave. Assuming a *Gaussian* feature of their probing beam, comparison of their data with our analysis, **Fig. A4**, shows close agreement when we assume *Gaussian* lateral profiles for their density waves too, with ≈ 2.8 cm full half widths (the discharge tube having 5. cm and the exciting grid 3. cm diameter).
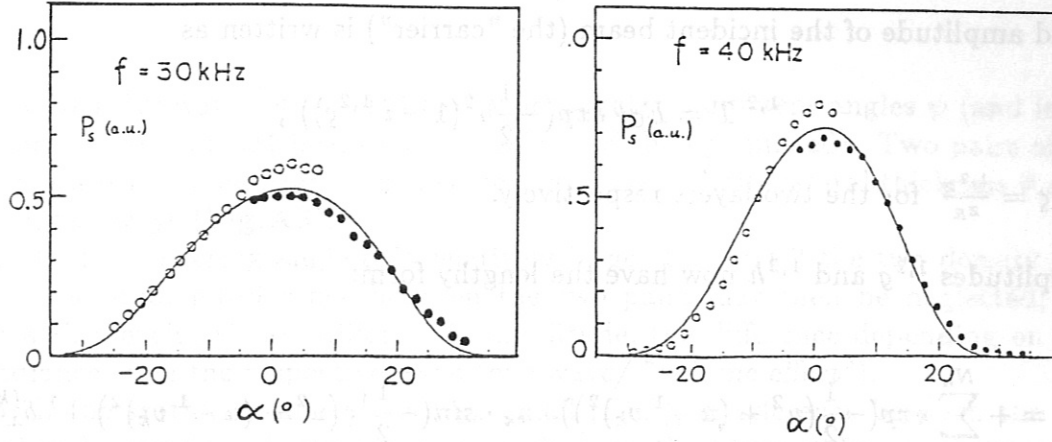
Fig. A4:
The right sideband peak amplitude I_{max} as a function of the angle of irradiation ψ_c,
measured by scattering of $\lambda = 0.875$ cm microwaves from ion acoustic waves
travelling axially in a cylindrical glow discharge, publ. 1973 by Tsukishima et al. /16/.
This is their fig.5, supplemented by a fitting curve of our model;
their angle α is related to our angle ψ_c by $\alpha = \psi_c - \psi_{Bragg}$ with ψ_{Bragg} the Bragg angle.

The data (left/right): $f = 30/40\,KHz$; $\Lambda = 2.25/1.80\,cm$; $\psi_{Bragg} = 11°/14°$.
Fitting with a thickness $\delta = 1.2/1.6$ amounts to a radial profile
of the density wave fronts that is gaussian in shape and $L \approx 2.8$ cm wide.

A4.

Equations (10) to (13) for one sheath are now replaced by

$$^1\delta_\pm^{(k)} = \pm \sum_{\kappa=k_c}^{k} {}^1\left(^{Bragg}\delta_\pm^{(k)}\right), \tag{19a}$$

$$^2\delta_\pm^{(k)} = \pm \sum_{\kappa=k_c}^{k} {}^2\left(^{Bragg}\delta_\pm^{(k)}\right) + \Delta; \tag{19b}$$

here is

$$^1\left(^{Bragg}\delta_\pm^{(k)}\right) = \frac{\Lambda_k}{\lambda} \cdot \left(\frac{\Lambda_k}{\lambda} 2\sin^2\left(\frac{^1\alpha_k}{2}\right) \mp \sin(^1\psi_k)\right) \cdot \cos^2(^1\psi_k) \cdot ^1\gamma_k, \tag{20a}$$

$$^2\left(^{Bragg}\delta_\pm^{(k)}\right) = \frac{\Lambda_k}{\lambda} \cdot \left(\frac{\Lambda_k}{\lambda} 2\sin^2\left(\frac{^2\alpha_k}{2}\right) \pm \sin(^2\psi_k)\right) \cdot \cos^2(^2\psi_k) \cdot ^2\gamma_k. \tag{20b}$$

(The reversed signs in the *Bragg*-phases in eqs. (20) are due to the fact that both the sign of the angle of incidence ψ and the direction of **K** change.) In this tiresome procedure of setting superscripts and subscripts do $^{1,2}\alpha_k$, $^{1,2}v_k$ and $^{1,2}\gamma_k$ of course have meanings analogous to those in eq. (11):

$$^{1,2}\gamma_k = (^{1,2}v_k)^2 \cdot \frac{L}{z_R \cdot \cos(^{1,2}\psi_k)} \quad, \text{ with } \quad v_k = \frac{2\pi w_0}{\Lambda_k \cdot \cos(^{1,2}\psi_k)}.$$

The field amplitude of the incident beam (the "carrier") is written as

$$^{1,2}T = E_0 \cdot exp\left(-\frac{1}{2}u^2(1 - i\ ^{1,2}\varsigma)\right),$$

with $^{1,2}\varsigma = \frac{^{1,2}z}{z_R}$ for the two layers respectively.

The amplitudes $^{1,2}g$ and $^{1,2}h$ now have the lengthy form:

$$^1g = +\sum_{k=1}^{N_n} exp\left(-\frac{1}{2}(u^2 + (u - ^1v_k)^2)\right) \cdot a_k \cdot sin\left(-\frac{1}{2}\ ^1\varsigma(u^2 - (u - ^1v_k)^2) + ^1\delta_+^{(k)}\right)$$

$$+\sum_{k=1}^{N_n} exp\left(-\frac{1}{2}(u^2 + (u + ^1v_k)^2)\right) \cdot a_k \cdot sin\left(-\frac{1}{2}\ ^1\varsigma(u^2 - (u + ^1v_k)^2) + ^1\delta_-^{(k)}\right),$$

$$^2g = +\sum_{k=1}^{N_n} exp\left(-\frac{1}{2}(u^2 + (u - ^2v_k)^2)\right) \cdot a_k \cdot sin\left(-\frac{1}{2}\ ^2\varsigma(u^2 - (u - ^2v_k)^2) + ^2\delta_+^{(k)}\right)$$

$$+\sum_{k=1}^{N_n} exp\left(-\frac{1}{2}(u^2 + (u + ^2v_k)^2)\right) \cdot a_k \cdot sin\left(-\frac{1}{2}\ ^2\varsigma(u^2 - (u + ^2v_k)^2) + ^2\delta_-^{(k)}\right),$$

$$^1h = +\sum_{k=1}^{N_n} exp\left(-\frac{1}{2}(u^2 + (u - ^1v_k)^2)\right) \cdot a_k \cdot cos\left(-\frac{1}{2}\ ^1\varsigma(u^2 - (u - ^1v_k)^2) + ^1\delta_+^{(k)}\right)$$

$$-\sum_{k=1}^{N_n} exp\left(-\frac{1}{2}(u^2 + (u + ^1v_k)^2)\right) \cdot a_k \cdot cos\left(-\frac{1}{2}\ ^1\varsigma(u^2 - (u + ^1v_k)^2) + ^1\delta_-^{(k)}\right),$$

$$^2h = +\sum_{k=1}^{N_n} exp\left(-\frac{1}{2}(u^2 + (u - ^2v_k)^2)\right) \cdot a_k \cdot cos\left(-\frac{1}{2}\ ^2\varsigma(u^2 - (u - ^2v_k)^2) + ^2\delta_+^{(k)}\right)$$

$$-\sum_{k=1}^{N_n} exp\left(-\frac{1}{2}(u^2 + (u + ^2v_k)^2)\right) \cdot a_k \cdot cos\left(-\frac{1}{2}\ ^2\varsigma(u^2 - (u + ^2v_k)^2) + ^2\delta_-^{(k)}\right).$$

(The profile shape a_k has assumed to be the same at both intersections.)

A5.

Two density waves of equal Ω and Λ propagate at different angles ψ (and in opposite directions) across an EM beam (the subscipts "c" being omitted). Two pairs of EM-field sidebands are scattered from these two density waves. Finite lateral thickness ϑ affects the result in two ways (**Fig.A5**):

a) If the scattering angle α is relatively large (FS) and if the two density waves are locally separated, interference between the two pairs may then be neglected; the sidebands within each pair are different in amplitude, the difference depending on the angle of irradiance ψ on the respective wave (*one wave/ "volume effect"*).

b) If the scattering angle α is very small (FFS), interference between the two pairs must then be considered, the result depending on the phase difference between the two density waves; in this case the sidebands within each of the two pairs are almost equal in amplitude (unless ϑ largely exceeds the order of 1); but they differ between the two pairs if the angles of irradiance ψ_1 and ψ_2 are different. Thus even when the amplitudes of both density waves are equal, the scattered field amplitudes are not (*two waves/ "counter-propagation"*).

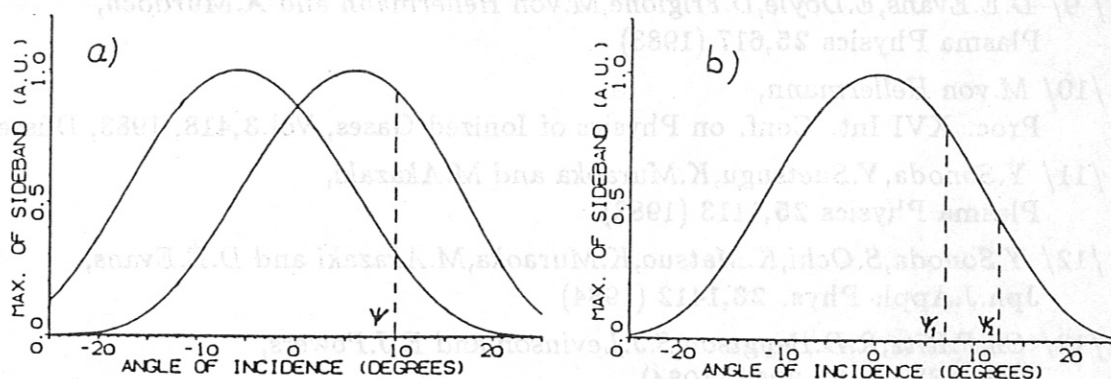Both effects cause an asymmetry of the resulting **K**-space profile: **Fig.A5**

Fig. A5: *The maxima of the two pairs of sidebands as functions of ψ, the angle of irradiation, for scattering from two locally separated density waves of wavelength Λ and of finite thickness ϑ, with $\Lambda = 1$ cm, $\vartheta = 2$ for each wave.*
a) *Probing wavelength $\lambda = 0.2$ cm ($\rightarrow$ scattering angle $\alpha = 11.7\,°$):*
   the amplitudes within each of the two pairs are different, the difference depending on ψ
b) *Probing wavelength $\lambda = .001$ cm ($\rightarrow$ scattering angle $\alpha = 0.06\,°$):*
   the amplitudes within each of the pairs are nearly equal
   (the traces for the pair of sidebands coincide),
   but they differ between both pairs if ψ_1 and ψ_2 are different.

/ 1/ J.C.Forster,P.M.Schoch,R.L.Hickok and W.C.Jennings,
Texas Univ.(Austin) Fusion Research Center Report, 1988

/ 2/ P.C.Liewer,
Nucl. Fus. **25**,543 (1985)

/ 3/ G.Müller,
Verhandl. d. DPG **18**,430 (1983) - (P136 in Regensburg)
Verhandl. d. DPG **21**,106 (1986) - (P136 in Stuttgart)

/ 4/ H.J.Meyer and C.Mahn,
Phys. Rev. Lett. **46**,1206 (1981)

/ 5/ G.Grieger et al.,
Plasma Physics and Contr. Fus. **28**,43 (1986)

/ 6/ H.Wobig et al.,
Nucl. Fus. Suppl. 1987, IAEA-CN-47/D-I-2 (Kyoto)

/ 7/ D.E.Evans,M.von Hellermann and E.Holzhauer,
Plasma Physics **24**,819 (1982)

/ 8/ M.von Hellermann,
Habilitationsschrift, Fachbereich Physik der Universität Essen, 1985

/ 9/ D.E.Evans,E.Doyle,D.Frigione,M.von Hellermann and A.Murdoch,
Plasma Physics **25**,617 (1983)

/10/ M.von Hellermann,
Proc. XVI Int. Conf. on Physics of Ionized Gases, Vol.**3**,418, 1983, Düsseldorf

/11/ Y.Sonoda,Y.Suetsugu,K.Muraoka and M.Akazaki,
Plasma Physics **25**,1113 (1983)

/12/ Y.Sonoda,S.Ochi,K.Matsuo,K.Muraoka,M.Akazaki and D.E.Evans,
Jpn.J.Appl. Phys. **23**,1412 (1984)

/13/ Ch.P.Ritz,R.D.Bengtson,S.J.Levinson and E.J.Powers,
Phys. Fluids **27**,2956 (1984)

/14/ D.L.Brower,W.A.Peebles,N.C.Luhmann,Jr. and R.L.Savage,Jr.,
Phys. Rev. Lett. **54**,689 (1985)

/15/ H.Weisen,Ch.Hollenstein and R.Behn,
Plasma Physics and Contr. Fus. **30**,293 (1988)

/16/ A.Mase,T.Yamamoto and T.Tsukishima,
Jap. J. Appl. Physics **13**,1266 (1974)

/17/ H.Renner et al.,
Controlled Fusion and Plasma Heating, EPS-Conference Schliersee,
Europhysics Conference Abstracts 10C, Part 1,287, 1986

/18/ sl J.R. Wolberg, "Prediction Analysis", Princeton 1967

/19/ H.W.H.van Andel,A.Boileau and M.von Hellermann,
Plasma Physics and Contr. Fus. **29**,49 (1987)

/20/ E.Holzhauer and J.H.Massig,
Plasma Physics **20**,867 (1978)